Slc4a11 Gene Disruption in Mice
CELLULAR TARGETS OF SENSORINEURONAL ABNORMALITIES*

Ivan A. Lopez[‡], Mark I. Rosenblatt[§1], Charles Kim[§2], Gary C. Galbraith[¶], Sherri M. Jones[‖], Liyo Kao[**], Debra Newman[**], Weixin Liu[**], Stacey Yeh[**], Alexander Pushkin[**], Natalia Abuladze[**], and Ira Kurtz[**3]

From [‡]Surgery, Division of Head and Neck, [¶]Psychiatry and Biobehavioral Sciences, and [**]Medicine, Division of Nephrology, David Geffen School of Medicine at UCLA, Los Angeles, California 90095, the [§]Margaret M. Dyson Vision Research Institute, Weill Cornell Medical College, New York, New York 10021, and the [‖]Department of Communication Sciences and Disorders, East Carolina University, Greenville, North Carolina 27858

NaBC1 (the *SLC4A11* gene) belongs to the SLC4 family of sodium-coupled bicarbonate (carbonate) transporter proteins and functions as an electrogenic sodium borate cotransporter. Mutations in *SLC4A11* cause either corneal abnormalities (corneal hereditary dystrophy type 2) or a combined auditory and visual impairment (Harboyan syndrome). The role of NaBC1 in sensory systems is poorly understood, given the difficulty of studying patients with NaBC1 mutations. We report our findings in $Slc4a11^{-/-}$ mice generated to investigate the role of NaBC1 in sensorineural systems. In wild-type mice, specific NaBC1 immunoreactivity was detected in fibrocytes of the spiral ligament, from the basal to the apical portion of the cochlea. NaBC1 immunoreactivity was present in the vestibular labyrinth, in stromal cells underneath the non-immunoreactive sensory epithelia of the macula utricle, sacule, and crista ampullaris, and the membranous vestibular labyrinth was collapsed. Both auditory brain response and vestibular evoked potential waveforms were significantly abnormal in $Slc4a11^{-/-}$ mice. In the cornea, NaBC1 was highly expressed in the endothelial cell layer with less staining in epithelial cells. However, unlike humans, the corneal phenotype was mild with a normal slit lamp evaluation. Corneal endothelial cells were morphologically normal; however, both the absolute height of the corneal basal epithelial cells and the relative basal epithelial cell/total corneal thickness were significantly increased in $Slc4a11^{-/-}$ mice. Our results demonstrate for the first time the importance of NaBC1 in the audio-vestibular system and provide support for the hypothesis that *SLC4A11* should be considered a potential candidate gene in patients with isolated sensorineural vestibular hearing abnormalities.

The SLC4 transporter family consists of proteins that mediate bicarbonate (carbonate) transport and include Cl-HCO_3 exchangers, Na/HCO_3 cotransporters, and sodium-driven Cl-HCO_3 exchangers (1). A single member of the family encoded by the *SLC4A11* gene does not transport bicarbonate (carbonate) (2, 3). On the basis of sequence homology with other members of the SLC4 family, the protein encoded by *SLC4A11* was initially called BTR1 (bicarbonate transporter 1) (2). Subsequently, motivated by its homology with the borate transporter BOR1 in *Arabidopsis* (4), experiments by Park *et al.* (3) reported that the transporter functioned in the presence of borate as an electrogenic sodium-borate cotransporter and was renamed NaBC1.

Mutations in the *SLC4A11* gene are responsible for corneal hereditary dystrophy type 2 (CHED2)[4] and Harboyan syndrome (5–14). In addition to corneal dystrophy, patients with Harboyan syndrome have perceptive hearing loss and nystagmus (7, 14). Whether all patients with CHED2 have undiagnosed hearing abnormalities is currently unknown. Heterozygous single nucleotide polymorphisms for *SLC4A11* have also been identified in Chinese and Indian patients with Fuchs dystrophy, the most common dystrophic cause of endothelial failure in the adult population. However, the mutations in the *SLC4A11* gene may only be responsible for about 5% of Fuchs cases, and causality has not yet been firmly established (13). No patients with *SLC4A11* mutations have been described with isolated hearing abnormalities. Moreover, whether NaBC1 plays a role in the vestibular system is unknown. Currently, the cellular targets and mechanisms, which have led to altered corneal and/or auditory function or development, have not been elucidated. To examine the role of NaBC1 in sensorineural tissues more precisely in a mammalian model system, we generated $Slc4a11^{-/-}$ mice and examined the histologic and functional abnormalities associated with the loss of NaBC1 expression.

EXPERIMENTAL PROCEDURES

Generation of $Slc4a11^{-/-}$ Mice—The research protocol for the use of animal subjects in this study was approved by the UCLA Animal Subject Protection Committee. Animals were handled and cared for in accordance with the Animal Welfare Act and in strict compliance with National Institutes of Health Guidelines. Mice deficient for $Slc4a11^{-/-}$ were generated by

[4] The abbreviations used are: CHED2, corneal hereditary dystrophy type 2; PBS, phosphate-buffered saline; ABR, auditory brainstem response; VsEP, vestibular evoked potential; DAPI, 4',6-diamidino-2-phenylindole; EEG, electroencephalographic.

infecting embryonic stem cells (129/SvEv[Brd]) with the retroviral gene trap vector VICTR48 (Lexicon Genetics), which integrated upstream of exon 2 (Fig. 1, *A* and *B*). The vector contains a splice acceptor, followed downstream by a neomycin resistance gene and polyadenylation sequence. The vector contains stop codons in all three reading frames, thereby terminating translation and preventing gene expression (15, 16). An embryonic stem cell line with the disrupted gene was injected into C57BL/6J blastocysts that were then implanted in pseudopregnant females. Offspring were crossed with C57BL/6J mice. Genotypes were determined by analysis of genomic DNA by PCR. Heterozygous mice were bred to homozygosity and used for genetic and phenotypic analysis. NaBC1 protein was detected in cochlea and cornea isolated from wild-type mice, whereas no NaBC1 protein was detected from $Slc4a11^{-/-}$ mice (Fig. 1*C*). Wild-type ($Slc4a11^{+/+}$), heterozygous ($Slc4a11^{+/-}$), and knock-out mice ($Slc4a11^{-/-}$) all had normal behavior, breeding, and growth. For *in vivo* experiments, mice were anesthetized with an intraperitoneal injection of a combination of ketamine (20 mg/kg; Phoenix Scientific, St. Joseph, MO) and xylazine (6 mg/kg; Phoenix Scientific). For terminal experiments, mice were sacrificed with a lethal dose of intraperitoneal pentobarbital (100 mg/kg; Abbott). Experiments were performed utilizing littermate controls for comparison.

Genotyping—Genomic DNA was isolated from the mouse tails using the GenElute Mammalian Genomic DNA Miniprep Kit (Sigma) according to the manufacturer's protocol. To detect the mutant alleles, the following primer pairs were used (product size 210 bp): 5′-AAATGGCGTTACTTAAGC-TAGCTTGC-3′ and 5′-GCAGCTCACAAATGCTAACTGT-AGCT-3′. Wild-type alleles were detected with the following primers (product size 400 bp): 5′-GTCGACTAAGGAGGCC-TTCCATCT-3′ and 5′-GCAGCTCACAAATGCTAACTG-TAGCT-3′.

Generation and Characterization of the C-terminal NaBC1 Antibody (CL-NaBC1)—A rabbit polyclonal antibody (CL-NaBC1) was generated against the murine NaBC1 C-terminal sequence: [844]CLPRIIEAKYLDVMDAEHRP[862]. This antibody was used in the immunoblotting and immunolocalization studies. NaBC1 (NM_032034) was amplified from human kidney cDNA and cloned into the PTT expression vector (17). The complete cDNA sequence was verified by DNA sequencing. To initially characterize the NaBC1 antibody, NaBC1 was expressed in HEK293 cells, using Lipofectamine 2000, and protein expression was assayed by immunocytochemistry and immunoprecipitation/immunoblotting. For this purpose, HEK293 cells were plated onto 100-mm dishes in 12 ml of Dulbecco's modified Eagle's medium, supplemented with 10% fetal bovine serum, 200 mg/liter L-glutamine, and penicillin/streptomycin. The cells were split onto plates with 1-inch coverslips, and 16 h postseeding, they were transfected with either a PTT plasmid containing NaBC1 or mock-transfected with the PTT plasmid alone following the manufacturer's instructions except that the transfection mixture was removed after a 2-h exposure. The cells were grown at 37 °C in a 5% CO_2 atmosphere and harvested 24–48 h post-transfection. Mock-transfected cells were used as a control. For immunocytochemistry studies characterizing the CL-NaBC1 antibody, the cells were rinsed with PBS (140 mM NaCl, 3 mM KCl, 6.5 mM Na_2HPO_4, 1.5 mM KH_2PO_4, pH 7.4), permeabilized with 1 ml of ice-cold methanol for 2 min, and then incubated with CL-NaBC1 antibody (1:100 dilution in PBS). After a 30-min incubation at room temperature, the cells were rinsed with PBS and further incubated with goat anti-rabbit IgG conjugated with Cy3 (1:500 dilution in PBS; Jackson ImmunoResearch) for 30 min at room temperature. The cells were then rinsed three times with PBS and mounted in Crystal/Mount (from Biomeda, Foster City, CA). Fluorescence images were acquired by a PXL charge-coupled device camera (model CH1; Photometrics) coupled to a Nikon Microphot-FXA epifluorescence microscope. Labeling of the cells with the NaBC1 antibody was blocked with specific immunizing peptide. As shown in Fig. 1*D*, NaBC1 immunoreactivity was detected in transfected HEK293 cells, whereas mock-transfected cells (Fig. 1, *E* and *F*) had no staining. Moreover, preincubation of the CL-NaBC1 antibody with the immunizing peptide blocked the cell staining (Fig. 1, *G* and *H*).

In separate experiments, the CL-NaBC1 antibody was further characterized by immunoprecipitation/immunoblotting of HEK293 cells transfected with the NaBC1 plasmid or mock-transfected cells. The cells were transfected in 100-mm dishes, as described above. After 24 h, the NaBC-transfected and mock-transfected cells were washed three times with ice-cold PBS and homogenized by passing 10 times through a 25-gauge needle (BD Biosciences) in 500 μl of lysis buffer (50 mM Tris·HCl, pH 7.5) containing 1 μg/ml pepstatin and complete Mini protease inhibitor mixture (1 tablet/2 ml; Roche Applied Science). Cell lysates were centrifuged at 600 × g for 10 min, and then the protein was extracted by using 1% of *n*-dodecyl-β-D-maltopyranoside (Anatrace, Maumee, OH) for 30 min at 4 °C. The protein samples were centrifuged at 15,000 × g for 5 min at 4 °C, and 2 μl of the CL-NaBC1 antibody were added and incubated at 4 °C with gentle agitation for 30 min. Protein A-Sepharose beads (GE Healthcare) were preblocked in lysis buffer containing bovine serum albumin (10 mg/ml) and 0.1% *n*-dodecyl-β-D-maltopyranoside for 1 h and were washed three times with lysis buffer containing 0.1% *n*-dodecyl-β-D-maltopyranoside. Protein samples were mixed with the protein A-Sepharose beads and incubated at 4 °C for 1 h with gentle agitation. The samples were washed three times with lysis buffer containing 0.1% *n*-dodecyl-β-D-maltopyranoside, and the protein was eluted with 4× SDS sample buffer containing 400 mM dithiothreitol (final concentration 2% SDS and 100 mM dithiothreitol) at 95 °C. The samples were analyzed by SDS-PAGE and immunoblotting. Protein samples were separated on 7.5% polyacrylamide gels (Jule, Milford, CT) and transferred to polyvinylidene difluoride membranes. Nonspecific binding was blocked with TBST (20 mM Tris-HCl, pH 7.5, 140 mM NaCl, and 0.1% Tween 20) with 5% dry milk and incubated for 1 h at room temperature. The primary Cl-NaBC1 antibody was used at a 1:1,000 dilution, and mouse anti-rabbit IgG was used at a 1:10,000 dilution. Both primary and secondary antibodies were incubated at room temperature for 1 h. Immunoblots were developed using an ECL kit and hyperfilm ECL (GE Healthcare). Moreover, preincubation of the CL-NaBC1 antibody with the immunizing peptide prevented immunoblot detection of NaBC1 (Fig. 1*C*).
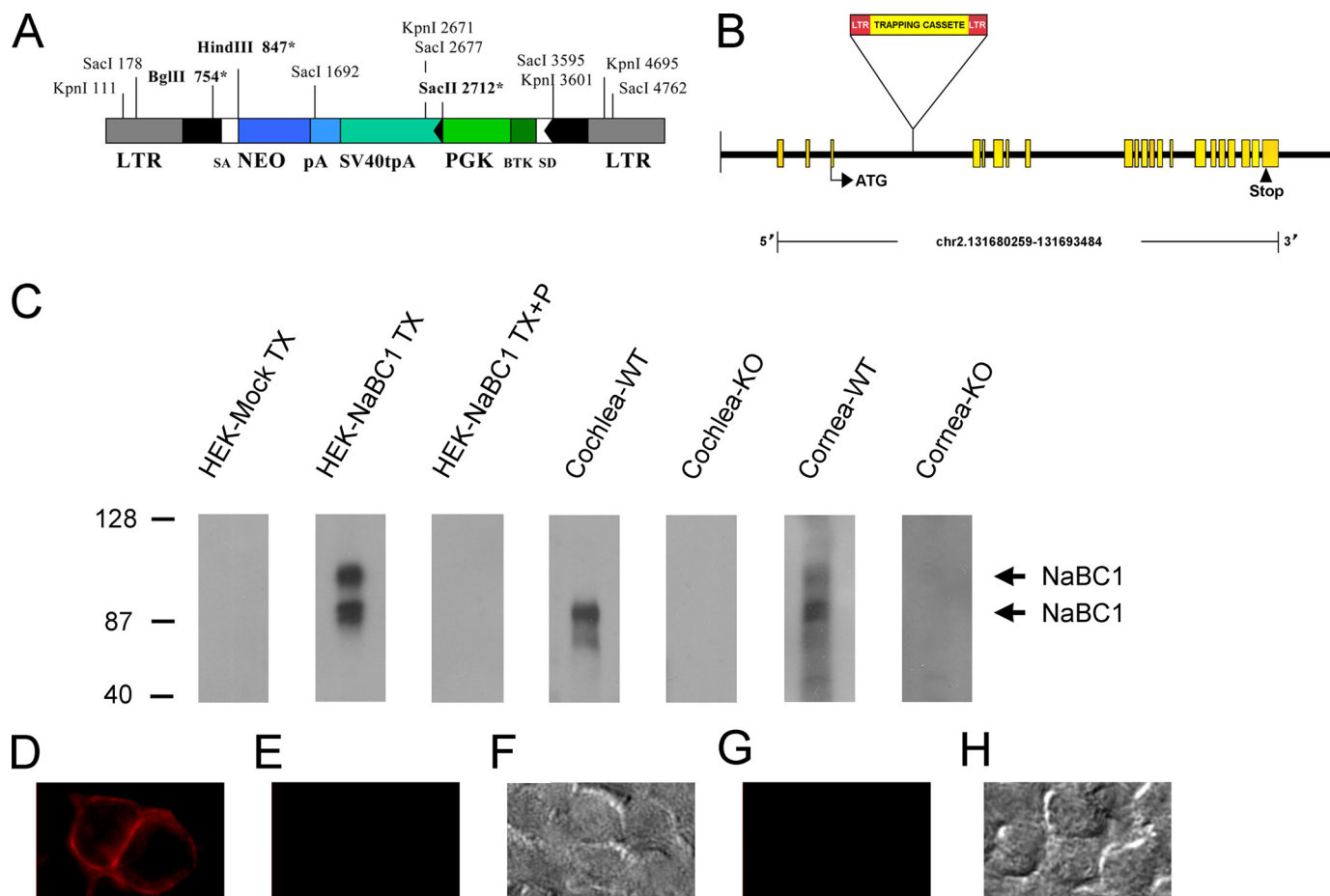
FIGURE 1. **Insertional deletion of *Slc4a11*.** *A*, restriction map of the retroviral gene trap vector, VICTR48. *B*, structural arrangement of 129 Sv/Ev[brd] mouse gene *Slc4a11*; diagram of the mutated *Slc4a11* allele after insertion. *C*, immunoblot analysis of protein samples prepared from HEK293 cells transfected with wild-type NaBC1, cochlea, and cornea of wild-type (*Slc4a11*^{+/+}), and knock-out (*Slc4a11*^{−/−}) mice using the C-terminal antibody to CL-NaBC1. *D*, HEK293 cells transfected with wild-type NaBC1, showing NaBC1 immunoreactivity. *E*, mock-transfected HEK293 cells showing lack of NaBC1 staining; *F*, Nomarski image of the same field in *E*. *G*, HEK293 cells transfected with wild-type NaBC1 were not stained when the Cl-NaBC1 antibody was preincubated with the immunizing peptide. *H*, Nomarski image of the same field in *G*. *LTR*, long terminal repeat.

Inner Ear Histology, Immunohistochemistry, and Immunoprecipitation/Immunoblotting—Mice were overanesthetized and decapitated, the brain was dissected from the head, and the temporal bones containing the cochlea were removed from the skull. For each animal, one cochlea was used for morphological analysis, and the other was used for immunohistochemistry. Cochleas were postfixed in a solution containing 2% glutaraldehyde, 4% paraformaldehyde (EMS, Worthington, PA) for 1 day. Thereafter, cochlea were immersed in 1% osmium tetroxide solution (EMS) for 1 h, washed with sodium phosphate buffer solution, and placed in a decalcifying solution containing 3% EDTA in PBS for 3 days. The cochleas were dehydrated with ascending alcohols and propylene oxide, infiltrated, and embedded in EPON-810 (Fluka, Germany). 5-μm-thick sections at the midmodiolar level were obtained using an ultramicrotome (Microm HM355S). Sections were counterstained with 1% toluidine blue solution and permanently mounted with Permount (Fisher).

For immunohistochemistry, cochleas were immersed in 4% paraformaldehyde solution for 3–4 h and decalcified by immersing them in 3% EDTA diluted in PBS for 3 days. Thereafter, cochleas were immersed in 30% sucrose dissolved in PBS for 5–7 days and then infiltrated with O.C.T. compound (Tis-

sue-Tek) as described (18). *Slc4a11*^{−/−} and *Slc4a11*^{+/+} mouse cochlea were mounted (adjacently) in the same cryostat holder, and 14-μm thick cryostat sections were obtained (Microm HN550). Sections were mounted on Superfrost plus glass slides (Fisher) and stored at −80 °C until their use.

Cochlea sections were incubated at room temperature for 1 h with a blocking solution containing 1% bovine serum albumin (Fraction V; Sigma) and 1% Triton X-100 (Sigma) diluted in PBS. Next, the blocking solution was removed, and the tissue sections were incubated in a humid chamber at 4 °C for 48 h with the CL-NaBC1 antibody (1:1000). At the end of the incubation, tissue sections were washed three times for 10 min each in PBS. A secondary Alexa 594 antibody (diluted 1:1000 in PBS; Molecular Probes) was applied and incubated for 1 h at room temperature in the dark. For cochlin staining, goat polyclonal cochlin antibody D-19 (1:1000; Santa Cruz Biotechnology, Santa Cruz CA) was utilized and detected with donkey and goat antibody labeled with Alexa 488 (1:1000; Molecular Probes).

At the end of antibody incubation, tissue sections were washed with PBS and mounted with Vectashield solution containing DAPI to visualize all cell nuclei (Vector Laboratories). The mixture was placed at 37 °C for 1 h, after which immunohistochemistry analysis was performed. Immunostained or

toluidine blue-stained tissue sections were viewed and imaged in an Eclipse E800 fluorescent microscope (Nikon, Tokyo, Japan) equipped with an RTSlider spot digital camera and Image Pro Plus™ software. To provide unbiased comparisons of the immunofluorescent signal from a particular antibody between each type of specimen, all images were captured using strictly the same camera settings. Morphological or immuno-histochemical data were obtained from at least six cochleas from six different $Slc4a11^{-/-}$ and $Slc4a11^{+/+}$ mice.

For immunoprecipitation/immunoblotting experiments, dissected $Slc4a11^{+/+}$ and $Slc4a11^{-/-}$ mouse cochlea were resuspended in 500 μl of lysis solution (50 mM Tris·HCl, pH 7.5) containing 1 μg/ml pepstatin and complete Mini protease inhibitor mixture (1 tablet/2 ml; Roche Applied Science) and disrupted in a glass homogenizer. The tissue was then homogenized by passing 40 times through a 25-gauge needle (BD Biosciences), centrifuged at 600 $\times$ *g* for 10 min, and processed for immunoprecipitation/immunoblotting, as described above.

Auditory Brainstem Response (ABR) Test—$Slc4a11^{-/-}$ and $Slc4a11^{+/+}$ mice were anesthetized with isoflurane gas (2% delivered with oxygen at 1 liter/min). Grass Medical Instruments (Quincy, MA) subdermal needle electrodes were then positioned behind and at the base of each pinnae ("transverse" channel) and on the scalp midline symmetrically located anterior and posterior to the interaural line ("midline" channel) at a distance approximately equivalent to that of the transverse channel (19). The acoustic stimulus consisted of a 16-kHz tone pip, 1-ms duration, and 0.5-ms linear rise/fall. The stimulus repetition rate was 11/s. Sound was delivered monaurally via an air tube placed into the ear canal and secured with beeswax, which served the dual purpose of cupping the pinnae around the tube and holding the tube firmly in place. The air tube length plus the internal sound path of an Intelligent Hearing Systems (Miami, FL) high frequency tone generator resulted in an acoustic conduction delay of 1 ms. This guaranteed that sound arrived at the ear canal immediately after possible electrical artifacts due to the 1-ms stimulus. A Berkeley Nucleonics Inc. (San Rafael, CA) model 630 arbitrary function generator running at an internal clock rate of 1.25 MHz delivered the digital stimulus waveform. Responses were recorded at peak stimulus intensities of 75, 65, and 55 db.

Transverse and midline bipolar electroencephalographic (EEG) activity was led to two Grass P511 amplifiers (gain 200,000$\times$, band pass 10,000–30,000 Hz, -6 db down). EEG recording quality was monitored continuously on a two-channel oscilloscope. Each epoch of sampled data were also displayed on a computer screen. The arbitrary function generator was triggered at the onset of each epoch and delivered the stimulus independent of computer sampling of the data. The two EEG channels were sampled at a rate of 100,000/s by a Scientific Solutions Lab Master analog-to-digital converter (Mentor, OH). The total sample epoch was 6.4 ms, including the initial 1 ms (100 data points) of stimulus artifact.

Custom data acquisition software developed for our murine ABR studies implemented effective on-line artifact rejection. This was accomplished by sampling the ongoing EEG prior to beginning the actual experiment and adjusting amplitude rejection thresholds against which all real time data samples were compared. All experimental trials containing extreme amplitudes, most often the result of heart rate activity, were rejected, and the stimulus was repeated.

Prior to the collection of each individual ABR average, the ongoing EEG was again sampled (at a reduced rate of 1,000/s) and displayed. A computer program automatically detected heartbeats in the sample and computed the average interbeat interval and the reciprocal heart rate. Heart rate values were then saved in conjunction with each averaged ABR as a measure of the animal's current physiological status. Averaged evoked responses were computed in real time based on 500 artifact-free trials. Final averaged ABR waveforms were displayed and saved for later off-line analysis. The latency analysis reported here consisted of positioning cursors on P1 of the transverse and midline ABR. The cursor positions defined the absolute peak latencies (taking into account the 1-ms acoustic delay). ABR amplitude was defined as the largest peak-to-trough component occurring within the first 4.0 ms of the response. The experimenters analyzing the data were always blind to animal genotype and age. The results were plotted and entered into Excel spreadsheets for later identification of genotype and age and subsequent statistical analyses. Comparison of the two independent groups, three age ranges, and latency differences between channels within the same animals was by a $2 \times 3 \times 2$ repeated measure analysis of variance. ABR amplitude was analyzed by a 2×3 analysis of variance (group $\times$ age, for the transverse channel only). Age groupings were 5–6 months ("young"), 7 months ("middle"), and 13–15 months ("old").

Balance Behavior—Cage behavior was observed for any signs of hyperactivity (running in circles) or unusual head or body postures. Drop reflexes were observed while each mouse was held by the tail and lowered to the surface of the tabletop. Normal reflexes were scored if the animal extended its forepaws toward the table surface. Reflexes were judged as abnormal if the forepaws remained flexed toward the body and were not extended toward the table top. Swimming behavior was also observed. Animals were suspended by the tail 2–3 inches above the surface of a small tank filled with tepid water. The animal was then dropped into the water and submerged beneath the surface. Swimming was determined to be normal if the mouse rose to the surface of the water, maintained its head above the surface and a horizontal body line in the water, and swam using its tail as a rudder. Abnormal swimming was noted if the animal remained submerged unable to find the surface or was disoriented such that the mouse swam to the surface momentarily but resubmerged often. With abnormal swimming, the animal must be removed from the water to prevent drowning.

Vestibular Evoked (VsEP) Potential Test—VsEP recordings followed methods reviewed by Jones (20) and Jones and Jones (21) and are briefly described here. The use of animals was approved by the Institutional Animal Care and Use Committee at East Carolina University. 5–7-month-old $Slc4a11^{+/+}$ (*n* = 14), and $Slc4a11^{-/-}$ (*n* = 9) were tested. Mice were anesthetized with a ketamine and xylazine mixture (18:2 mg/ml; intraperitoneal injections of 6 μl/g body weight). Core body temperature was maintained at 37.0 $\pm$ 0.2 °C using a homeothermic heating blanket system (FHC).

Linear acceleration pulses, 2-ms duration, were presented to the cranium in the naso-occipital axis using two stimulus polarities, normal and inverted. Stimuli were presented at a rate of 17 pulses/s. Stimulus amplitude ranged from +6 db to −18 db reference 1.0 g/ms (where $1 g = 9.8$ m/s^2) adjusted in 3-db steps. Stimuli were delivered to the head using a voltage-controlled mechanical shaker. The head was coupled to a custom platform with a custom head clip. The head clip was a lightweight plastic spring hair clip with tines modified to encircle the head anterior to the pinnae. The spring clip was screwed to the platform mounted to a mechanical shaker (Labworks).

Stainless steel wire was placed subcutaneously at the nuchal crest to serve as the non-inverting electrode. Needle electrodes were placed posterior to the right pinna and at the hip for inverting and ground electrodes, respectively. Traditional signal averaging was used to resolve responses in electrophysiological recordings. Ongoing electroencephalographic activity was amplified (200,000×), filtered (300–3,000 Hz, −6 db amplitude points), and digitized (1024 points, 10 μs/point). 256 primary responses were averaged for each VsEP response waveform. All responses were replicated. Recordings began at the maximum stimulus intensity (*i.e.* +6 db reference 1.0 g/ms) with and without acoustic masking, and then intensity was dropped to −18 db and raised in 3-db steps to complete an intensity profile. Acoustic masking (broad band forward masker, 50–50,000 Hz, 97 db sound pressure level) was presented during VsEP measurements to verify the absence of cochlear responses.

The first three positive and negative response peaks were scored. The first response peak (*i.e.* P1 and N1) was used for analyses, since this response peak represents compound neural activity from the peripheral vestibular nerve. Response peak latency for P1 (measured in ms), peak-to-peak amplitude for P1-N1 (measured in μV), and thresholds (measured in db reference 1.0 g/ms) were quantified. Descriptive statistics were generated for each genotype. Independent sample t tests were used to compare P1 latency, N1 latency, P1-N1 amplitude, and VsEP thresholds between wild types and homozygotes.

Cornea Histology, Immunohistochemistry, and Immunoblotting—$Slc4a11^{+/+}$ and $Slc4a11^{-/-}$ mice were anesthetized and subjected to slit lamp examination (Topcon). Corneas were examined and imaged (Nikon D1 Digital SLR) for anterior segment pathology using both broad diffuse illumination and tangential slit illumination. Following examination, mice were euthanized and enucleated. For hematoxylin and eosin staining, eyes were fixed overnight in 4% paraformaldehyde, followed by washing in PBS the next day. The tissue was then dehydrated through a series of ethanol and xylene solutions and embedded in Tissue Prep® paraffin wax (Fisher) in OmniSette® tissue cassettes (Fischer). 4-μm sections were cut onto Plus salinated slides (Fischer) and allowed to air-dry. Slides were placed on an automatic stainer by Sakura (model DRS-601; Sakura Finetek (Torrance, CA)) and coverslipped using TBS ShurMount permanent mounting medium (American Master*Tech Scientific, Lodi, CA). For endothelial cell staining, eyes were enucleated, and corneal whole mounts were dissected. Unfixed corneal tissue was stained with 1% alizarin red solution for 1 min and then rinsed with normal saline (22).

Mounting medium (Vectashield; Vector Laboratories) and coverslips were applied prior to imaging. Corneal sections stained for histology and alizarin red-stained whole mounts were imaged under bright field illumination using a motorized microscope (AxioVert 200 M, with Axiovision 4.0) equipped with a digital camera (Axiocam MRM), and images were processed using image analysis software (Axiovision 4.0; all were from Carl Zeiss Meditec, Oberkochen, Germany). In all cases, images were taken of representative sections corresponding to the central cornea.

Corneal endothelial and epithelial cells were counted within a 2×200-μm region in the central cornea following corneal extraction and staining. Only cells touching the left and upper boundaries were counted. All cells within the quantification area were manually traced, and the area of each cell was calculated using Axiovision 4.5 imaging software. A representative section taken from the central corneal region was selected for analysis. For each section, measurements of total corneal thickness were taken at five equally distributed points near the cornea center using Axiovision 4.5 software. The imaging analysis software was also used to take measurements of epithelial thickness at 10 equally distributed points and the height of 25 adjacent basal epithelial cells at the central cornea. Measurements were used to determine average central corneal thickness (t), average central epithelial thickness (e), and average central basal epithelial cell height (b). The ratio of average basal epithelial cell height to epithelial thickness (b/e) was also calculated for each section. Corneal parameters for $Slc4a11^{+/+}$ versus $Slc4a11^{-/-}$ mice were compared. Sigmastat was used to calculate differences between groups using Student's t test. A $p < 0.05$ value was considered significant.

To examine the immunolocalization of NaBC1 in the murine cornea, mice were anesthetized and then decapitated. Under the dissecting microscope, the whole eyes were carefully removed from the skull using microscissors and immersed immediately in 2% paraformaldehyde solution for 3–4 h. Thereafter, the whole eyes were immersed in 30% sucrose dissolved in PBS for 3 days and infiltrated with O.C.T. compound. $Slc4a11^{+/+}$ and $Slc4a11^{-/-}$ mice eyes were mounted (adjacently) in the same cryostat holder, and 10-μm thick cryostat (sagittal) sections were obtained (Microm, HN505E). Sections were mounted on Superfrost Plus glass slides (Fisher Scientific) and stored at −80 °C until their use. The immunohistochemistry studies using the CL-NaBC1 antibody were done as described above for the inner ear. The data were obtained from the observation of three eyes from three different $Slc4a11^{+/+}$ and $Slc4a11^{-/-}$ mice. In separate experiments, dissected $Slc4a11^{+/+}$ and $Slc4a11^{-/-}$ mouse corneas were suspended in 500 μl of lysis solution (50 mM Tris·HCl, pH 7.5, 1 μg/ml pepstatin, and complete Mini protease inhibitor mixture (1 tablet/2 ml; Roche Applied Science) and processed for immunoprecipitation/immunoblotting, as described above.

RESULTS

Cochlea and Vestibular Cellular Morphology—Midmodiolar sections of $Slc4a11^{-/-}$ mouse cochlea showed an overall normal organization (Fig. 2). Specifically, inner and outer hair cells in the organ of Corti had a normal appearance (Fig. 2, *D*
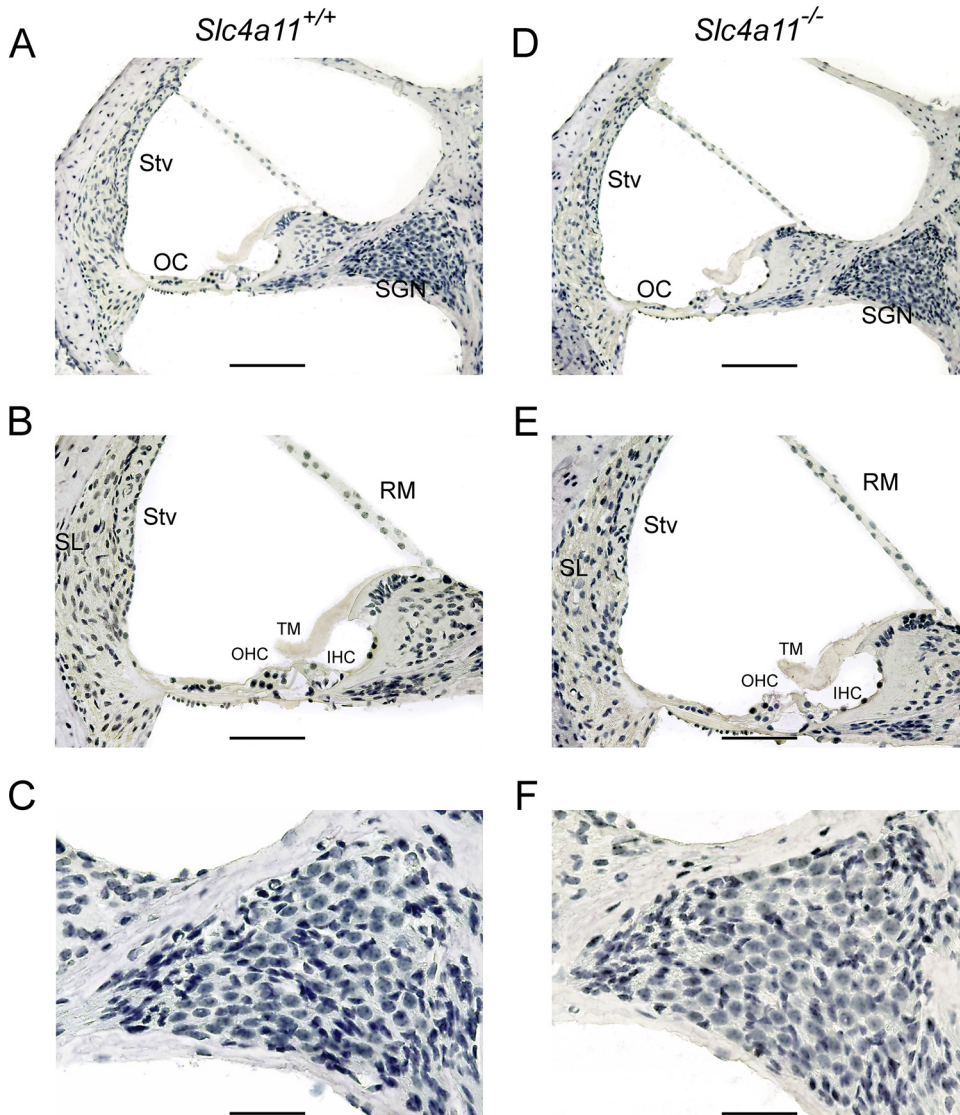
FIGURE 2. **The cochlea of the *Slc4a11*^{+/+} and *Slc4a11*^{−/−} mice.** *A*, low magnification view from the *Slc4a11*^{+/+} mouse cochlea. *B*, higher magnification view of the *Slc4a11*^{+/+} mouse cochlea. *C*, the normal spiral ganglia neurons (*SGN*) in *Slc4a11*^{+/+} mice. *D*, low magnification view from the *Slc4a11*^{−/−} mouse cochlea. *E*, higher magnification of the *Slc4a11*^{−/−} mouse cochlea. The inner (*IHC*) and outer hair cells (*OHC*) in the organ of Corti (*OC*) have a normal appearance. The stria vascularis (*Stv*), Reissner's (*RM*), and tectorial membrane (*TM*) were also normal. The spiral ligament (*SL*) showed a normal complement of fibrocytes. *F*, the spiral ganglia neurons of *Slc4a11*^{−/−} mice. *A* and *D* were taken from similar cochlear regions (midbase). *Bar*, 100 μm (*A* and *D*), 50 μm (*B* and *E*), and 25 μm (*C* and *F*).

and *E*) as did the stria vascularis, Reissner's, and tectorial membranes (Fig. 2*D*). The spiral ligament showed a normal complement of type I, II, and IV fibrocytes in the *Slc4a11*^{−/−} mice (Fig. 2*E*). The spiral ganglia neurons in the *Slc4a11*^{−/−} mice were also normal without cellular loss or vacuolization (Fig. 2*F*). The organ of Corti and spiral ganglia neurons from a *Slc4a11*^{+/+} mouse are shown for comparison (Fig. 2, *A–C*). *A* and *D* of Fig. 2 were taken from similar cochlear regions (midbase).

Cross-sections of the vestibular end organs (crista ampullaris, macula utricle, and sacule) from *Slc4a11*^{−/−} mice showed normal morphology (Fig. 3, *D–E*); however, the membranous labyrinth that encases the sensory epithelia was collapsed. This morphology was consistently observed in six temporal bones from six *Slc4a11*^{−/−} mice. The *arrows* in

Fig. 3, *D–F*, indicate the collapse over the horizontal crista and utricle, posterior crista, and saccule, respectively. Vestibular ganglia neurons and their fibers were normal at all ages (not shown). Vestibular end organs (posterior crista, macula utricle, and sacule) from a representative *Slc4a11*^{+/+} mouse are shown for comparison (Fig. 3, *A–C*), illustrating the normal organization of the sensory epithelia and membranous labyrinth (*i.e.* no collapse or swelling).

NaBC1 Localization in the Cochlea and Vestibular Epithelium— NaBC1 expression was examined in *Slc4a11*^{+/+} and *Slc4a11*^{−/−} mice. Midmodiolar sections of the cochlea from *Slc4a11*^{+/+} mice showed a uniform pattern of NaBC1 immunoreactivity from the base to the apical portion of the cochlea in the spiral ligament (Fig. 4*A*). A higher magnification view of the organ of Corti showed specific NaBC1 immunoreactivity in the spiral ligament and also in cells of the spiral limbus (Fig. 4*B*). The stria vascularis, Reissner's membrane, inner and outer cells, as well as supporting cells were not immunoreactive. Spiral ganglia neurons were also not immunoreactive. In the *Slc4a11*^{−/−} mice cochlea, NaBC1 immunoreactivity was not present (Fig. 4*C*). A higher magnification view of these findings is shown in Fig. 4*D*.

NaBC1 immunoreactivity in vestibular end organs of *Slc4a11*^{+/+} mice was found in fibrocytes of the stroma underneath the non-immunoreactive sensory epithelia. Fig. 5*A* shows a cross-section of the sacule in *Slc4a11*^{+/+} mice. A similar pattern of immunoreactivity was seen in the macula, utricle, and crista (not shown). The transition epithelia or dark cells were also non-immunoreactive. Fig. 5*B* shows a cross-section of the sacule of *Slc4a11*^{−/−} mice. No NaBC1 immunoreactivity was seen in vestibular end organs in *Slc4a11*^{−/−} mice.

Colocalization of NaBC1 with Cochlin in Mouse Cochlea— Fig. 6*A* shows NaBC1 immunoreactivity in the spiral ligament of an *Slc4a11*^{+/+} mouse counterstained with antibodies against cochlin, the most abundant extracellular protein expressed in the inner ear. Note that NaBC1 is exclusively located in the fibrocytes. NaBC1 expression was seen in the five types of fibrocytes (I–V) of the spiral ligament. Fig. 6*B* shows a high magnification view of the spiral ligament from
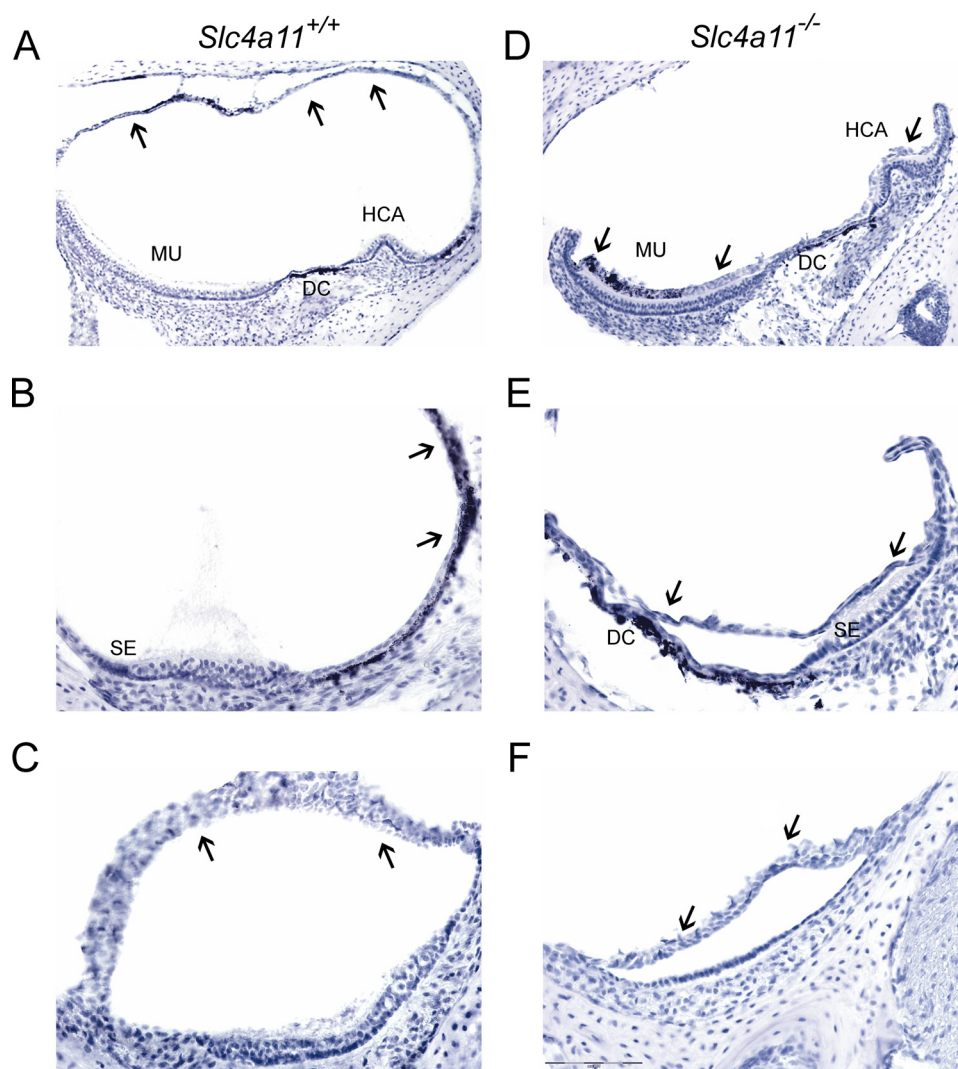
Slc4a11$^{+/+}$

Slc4a11$^{-/-}$

FIGURE 3. **The vestibular endorgans from *Slc4a11*$^{+/+}$ and *Slc4a11*$^{-/-}$ mice.** Shown are the macula utricle (*MU*) and horizontal crista ampullaris (*HCA*) (*A*) posterior crista (*B*), and macula sacule (*C*) of the *Slc4a11*$^{+/+}$ mouse. The *arrows* point to the normal appearance of the membranous labyrinth. *D*, in the *Slc4a11*$^{-/-}$ mouse, the membranous labyrinth was collapsed (*arrows*) over normal sensory epithelia (*SE*) of the macula utricle and horizontal crista ampullaris. *E*, collapse of the membranous labyrinth (*arrows*) in the posterior crista ampullaris. *F*, collapse of the membranous labyrinth (*arrows*) in the macula sacule. *Bar*, 100 μm (*A* and *D*) and 50 μm (*B*, *C*, *E*, and *F*).

an *Slc4a11*$^{-/-}$ mouse lacking NaBC1 staining. *Slc4a11*$^{-/-}$ mice showed no changes in cochlin immunoreactivity.

ABR Studies—Fig. 7 shows marked qualitative differences in ABR patterns obtained from three age groups of *Slc4a11*$^{+/+}$ and *Slc4a11*$^{-/-}$ mice. Traces are superimposed and plotted separately for the three peak stimulus intensities (75, 65, and 55 db). Thus, although *Slc4a11*$^{+/+}$ mice show measurable responses at all three stimulus intensities, *Slc4a11*$^{-/-}$ mice show a measurable response only at the highest (75 db) stimulus intensity. Fig. 7 does not plot data for the 55-db stimulus in *Slc4a11*$^{-/-}$ mice; ABRs to the 55-db stimulus were not recorded, since these animals failed to show measurable responses at the higher, 65-db, intensity. Moreover although a stable response pattern is well maintained across the three *Slc4a11*$^{+/+}$ age groups, as defined in terms of a high degree of intersubject consistency of ABR amplitudes, latencies, and overall waveform morphology, these features of the ABR

increasingly deteriorate for middle and old *Slc4a11*$^{-/-}$ mice. Indeed, even for the best defined response in *Slc4a11*$^{-/-}$ mice (75 db, ages 5–6 months), there is wide intersubject variability in ABR amplitude and latency. Such increased response variability and overall deterioration of the ABR confirms poor neural auditory coding in *Slc4a11*$^{-/-}$ mice.

Quantitative ABR latency measurements showed a consistent overall delay in the P1 component in the midline (mean = 1.02 ms) as compared with the transverse (mean = 0.88 ms) channel ($F(1,83) = 105.65$, $p < 0.001$). Such differences between transverse and midline latencies provide evidence that unique and independent neural processes are being measured, with the earliest transverse component reflecting activity in the auditory nerve and later midline waves reflecting activity farther along the central auditory pathway (19, 23). There was a significant overall effect of genotype ($F(1,83) = 11.37$, $p < 0.01$) due to longer latencies in *Slc4a11*$^{-/-}$ (mean = 1.02 ms) as compared with *Slc4a11*$^{+/+}$ (mean = 0.85 ms) mice (mean values averaged over three age ranges and two electrode channels). These results confirm an overall disruption of auditory processing in *Slc4a11*$^{-/-}$ mice. There was also a significant electrode × genotype interaction ($F(1,83) = 12.65$, $p < 0.001$). This was due to a reduced central conduction time (midline latency minus transverse latency) for *Slc4a11*$^{-/-}$ (1.06 − 0.97 = 0.09 ms) as compared with *Slc4a11*$^{+/+}$ (0.94 − 0.77 = 0.17 ms) mice. These results suggest that although *Slc4a11*$^{-/-}$ mice have longer latencies overall, especially in the transverse channel (0.97 *versus* 0.77 ms), nevertheless subsequent central conduction is relatively fast (0.09 *versus* 0.17 ms). Although there was an overall age effect ($F(2,83) = 4.44$, $p < 0.05$), the genotype × age interaction was not significant. Thus, within the range of ages tested here (5–15 months), we were unable to statistically substantiate a degenerative latency process in initial ABR latency for *Slc4a11*$^{-/-}$ animals. However, there were quite obvious age-related amplitude pattern changes in *Slc4a11*$^{-/-}$ mice (Fig. 7, *right*), with reduced amplitudes overall and a dramatic decrease in amplitude with increasing age. A statistical analysis of the largest ABR peak-to-trough amplitude (log-transformed) statistically corroborated these patterns. Thus, there were significant main effects for genotype
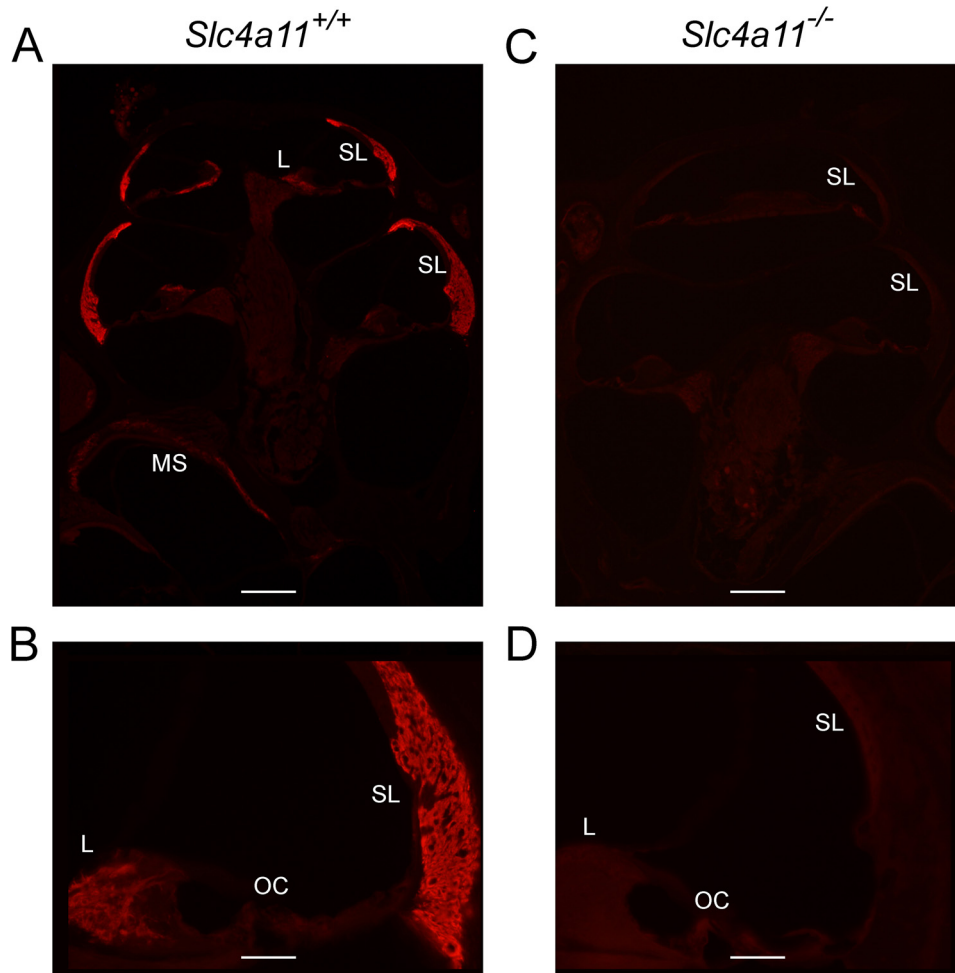
A *Slc4a11*$^{+/+}$

C *Slc4a11*$^{-/-}$

B

D

FIGURE 4. **NaBC1 immunofluorescence in *Slc4a11*$^{+/+}$ and *Slc4a11*$^{-/-}$ mice.** *A*, NaBC1 immunofluorescence in the spiral ligament (*SL*) of the cochlea from *Slc4a11*$^{+/+}$ mice. A uniform NaBC1 pattern was observed from the base to apical portion of the cochlea. *B*, higher magnification view shows specific NaBC1 immunofluorescence in the spiral ligament and the spiral limbus (*L*). The organ of Corti (*OC*) is devoid of any immunofluorescence signal. *C*, NaBC1 immunofluorescence was not detected in the *Slc4a11*$^{-/-}$ mouse cochlea. *D*, high magnification view to corroborate the lack of NaBC1 immunofluorescence. *Bar*, 250 μm (*A* and *C*) and 25 μm (*B* and *D*).

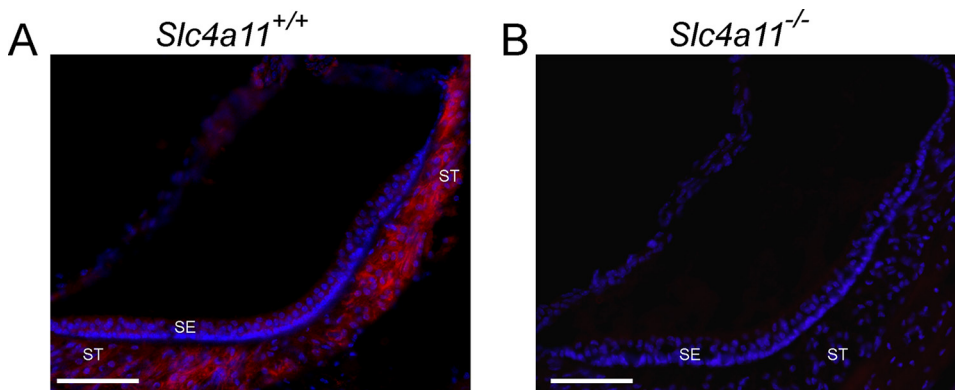**A** *Slc4a11*$^{+/+}$

B *Slc4a11*$^{-/-}$

FIGURE 5. **NaBC1 immunofluorescence in vestibular endorgans of the *Slc4a11*$^{+/+}$ and *Slc4a11*$^{-/-}$ mice.** *A* and *B*, cross-section of the macula sacule. *A*, NaBC1 immunofluorescence was located in the stroma (*ST*) underneath the sacule sensory epithelia (*SE*) of *Slc4a11*$^{+/+}$ mice. *B*, NaBC1 immunoreactivity was not detected in sensory epithelia or stroma of the macula sacule in *Slc4a11*$^{-/-}$ mice. DAPI (*blue*) shows cell nuclei. *Bar* in *A* and *B*, 100 μm.

latencies and amplitudes clearly indicate a significant disruption in auditory processing in *Slc4a11*$^{-/-}$ mice. Because the initial ABR component occurs with latency of 1 ms or less, and the observed amplitude differences occurred within the first several ms, these results necessarily point to the earliest stage(s) of auditory processing. Such impaired early processing in *Slc4a11*$^{-/-}$ mice implicates a disruption of neural transduction at the receptor level in the cochlea as well as possible further involvement of the eighth nerve.

Balance Behavior and VsEP Studies—All animals showed normal cage behavior, normal drop reflexes, and normal swimming. Balance behavior did not identify the animals as belonging to a particular genotype. Examples of typical VsEP waveforms in *Slc4a11*$^{+/+}$ and *Slc4a11*$^{-/-}$ mice are shown in Fig. 8. All *Slc4a11*$^{+/+}$ waveforms had normal appearing morphology with three distinct peaks occurring within 4 ms of stimulus onset. All *Slc4a11*$^{-/-}$ waveforms demonstrated substantially smaller peaks for P1 with prolonged latencies for peaks beyond P1 (Fig. 8). Indeed, three of the eight *Slc4a11*$^{-/-}$ mice did not have a distinguishable P1 response peak. Fig. 9*A* shows the mean VsEP latencies for response peaks P1 and N1, and Fig. 9*B* shows the mean P1-N1 amplitudes as a function of jerk amplitude. At the highest stimulus level presented (+6 db reference 1.0 *g*/ms), statistical analysis revealed no difference between *Slc4a11*$^{+/+}$ and *Slc4a11*$^{-/-}$ mice for P1 latencies; however, N1 latencies were significantly longer ($t(1,18) = -2.947$, $p = 0.014$) in *Slc4a11*$^{-/-}$ mice (1.60 ± 0.11 ms) compared with *Slc4a11*$^{+/+}$ mice (1.47 ± 0.07 ms). P1-N1 amplitudes were significantly smaller ($t(1,17) = 2.776$, $p = 0.013$) in *Slc4a11*$^{-/-}$ mice (0.41 ± 0.21 μV) compared with *Slc4a11*$^{+/+}$ mice (0.74 ± 0.25 μV). VsEP thresholds were significantly elevated in *Slc4a11*$^{-/-}$ mice with average thresholds of −6.4 ± 2.2 db reference 1.0 *g*/ms and −10.5 ± 1.2 db for *Slc4a11*$^{-/-}$ and *Slc4a11*$^{+/+}$ mice, respectively.

($F(1,79) = 29.37$, $p < 0.001$) and age ($F(2,79) = 11.26$, $p < 0.001$), as well as a significant genotype × age interaction ($F(2,79) = 4.96$, $p < 0.01$).

Taken together, the distinctive qualitative patterns seen in Fig. 7 and the corroborating quantitative analyses of ABR
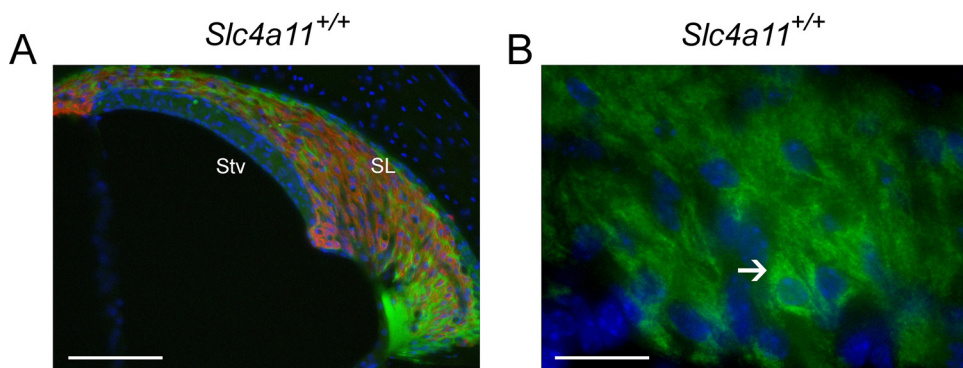
FIGURE 6. *A*, NaBC1 immunofluorescence in the spiral ligament (*SL*) (shown in *red*) simultaneously immunoreacted with antibodies against cochlin (shown in *green*) in the *Slc4a11*$^{+/+}$ mouse. NaBC1 is exclusively located in the fibrocytes, whereas cochlin is seen in the extracellular matrix. NaBC1 expression was seen in fibrocytes of the spiral ligament. The stria vascularis (*Stv*) did not stain for NaBC1. *B*, higher magnification view in the *Slc4a11*$^{+/+}$ mouse spiral ligament. NaBC1 immunoreactivity (in *green*) was present in the soma of fibrocytes (*arrow*). No immunoreactivity was seen in the nuclei (stained in *blue*). *Bar*, 25 μm (*A*) and 10 μm (*B*).
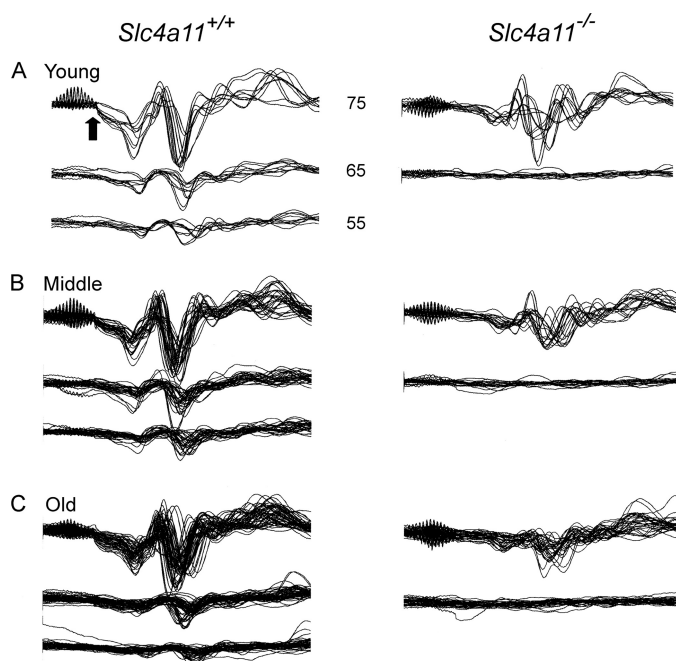

FIGURE 7. **Superimposed ABR waveforms for Slc4a11$^{+/+}$ (*left*) and Slc4a11$^{-/-}$ (*right*) mice (2 ABR replicates/animal).** Each cluster of three (*Slc4a11*$^{+/+}$) or two (*Slc4a11*$^{-/-}$) superimposed displays is ordered in decreasing stimulus level intensity (75, 65, and 55 db). The *vertical arrow* in the *upper left* marks the 1 ms end of stimulus artifact and actual arrival of sound at the ear. Age groupings are as follows. *A*, young (*Slc4a11*$^{+/+}$, 115–181 days; *Slc4a11*$^{-/-}$, 151–175 days); *B*, middle (*Slc4a11*$^{+/+}$, 204–211 days; *Slc4a11*$^{-/-}$, 200–211 days); *C*, old (*Slc4a11*$^{+/+}$, 398–464 days; *Slc4a11*$^{-/-}$, 386–455 days).

Slit Lamp Examination of the Cornea—Under broad beam illumination, the sclera, conjunctiva, and cornea of *Slc4a11*$^{+/+}$ and *Slc4a11*$^{-/-}$ mice were indistinguishable. The corneas of *Slc4a11*$^{-/-}$ mice were lustrous and clear, without evidence of edema or opacification (Fig. 10, *A* and *C*). Further examination using a tangentially directed slit beam demonstrated a transparent, compact corneal stroma in *Slc4a11*$^{-/-}$ mice, similar to their wild-type littermates (Fig. 10, *B* and *D*). Examination of mice at 3, 5, and 10 months of age ($n = 3$ at each time point) did not reveal any differences between age-matched *Slc4a11*$^{-/-}$ and *Slc4a11*$^{+/+}$ mice (data not shown). Therefore, the corneal

phenotype in *Slc4A11*$^{-/-}$ mice differ significantly from the severe corneal phenotype described in patients with mutations in the *SLC4A11* gene (5–14).

Cornea Cellular Morphology—In rder to examine potential subtle corneal abnormalities in *Slc4a11*$^{-/-}$ mice at the cellular level, corneal whole mounts were stained using alizarin red to visualize endothelial cell boundaries (Fig. 11*A* and *B*). The central corneal endothelial cell density was measured in mice ages 3–10 months and found to be 1650 ± 396 in *Slc4a11*$^{+/+}$ mice and 1795 ± 129 in *Slc4a11*$^{-/-}$ mice, which was not statistically different (p = not significant, Student's *t* test) (Fig. 11*C*). Endothelial cell size and shape in *Slc4a11*$^{+/+}$ and *Slc4a11*$^{-/-}$ mice were not significantly different. Quantitative analysis of average cell size was not statistically different between groups with an average endothelial cell size of 487 ± 100 μm^2 in *Slc4a11*$^{+/+}$ mice and 435 ± 27 μm^2 in *Slc4a11*$^{-/-}$ mice (Fig. 11*D*). No abnormalities were detected in Descemet's membrane.

However, an altered architecture of the basal epithelial layer was present in *Slc4a11*$^{-/-}$ mice. Specifically, the basal epithelial cells assumed a more columnar morphology as compared with cells observed in *Slc4a11*$^{+/+}$ mice (Fig. 12). The central corneal thickness (Fig. 12, *A* and *D*) of *Slc4a11*$^{+/+}$ mice (139 ± 12 μm) and *Slc4a11*$^{-/-}$ mice (137 ± 24 μm) were not significantly different. Similarly, the total epithelial thickness (Fig. 12*B*) of *Slc4a11*$^{+/+}$ (36 ± 3.6 μm) and *Slc4a11*$^{-/-}$ mice (37 ± 2.8 μm) did not differ significantly. In contrast, the basal epithelial cell height (Fig. 12, *B*, *C*, and *F*) of *Slc4a11*$^{-/-}$ mice (17.9 ± 1.2 μm) was significantly greater ($p < 0.001$) than that of *Slc4a11*$^{+/+}$ mice (15.2 ± 0.45 μm). In order to ameliorate any effect of total epithelial thickness on the comparison of basal cell height, the ratio of basal height (*b*) to the epithelial thickness was calculated (*e*). With this correction, we still observed a basal epithelial cell height; *Slc4a11*$^{-/-}$ mice (0.48 ± 0.025) *versus* *Slc4a11*$^{+/+}$ mice (0.42 ± 0.049), $p < 0.025$ (Fig. 12*G*).

NaBC1 Localization in the Cornea—NaBC1 expression was examined in *Slc4A11*$^{+/+}$ and *Slc4A11*$^{-/-}$ mice. Sagittal sections of the central portion of cornea from *Slc4a11*$^{+/+}$ mice showed a uniform pattern of NaBC1 immunoreactivity in the endothelial cell layer (Fig. 13*A*). Less pronounced NaBC1 immunoreactivity was also seen in the epithelium layer. The stroma in *Slc4a11*$^{+/+}$ mice was not immunoreactive to the CL-NaBC1 antibody, with DAPI cell nuclear staining revealing the normal organization pattern of cells in the stromal layers (*i.e.* parallel-longitudinal arrays) (Fig. 13*B*). Fig. 11*C* shows a *merged image* from Fig. 13, *A* and *B*. In the cornea of *Slc4A11*$^{-/-}$ mice, no specific immunoreactivity for NaBC1 was detected (Fig. 13*D*). In addition, as shown in Fig. 13*E*, the cells within the stroma of *Slc4a11*$^{-/-}$ mice were more disorganized than in *Slc4a11*$^{+/+}$ mice (Fig. 13*B*). Fig. 13*F* shows a *merged image* of Fig. 3, *D* and *E*.
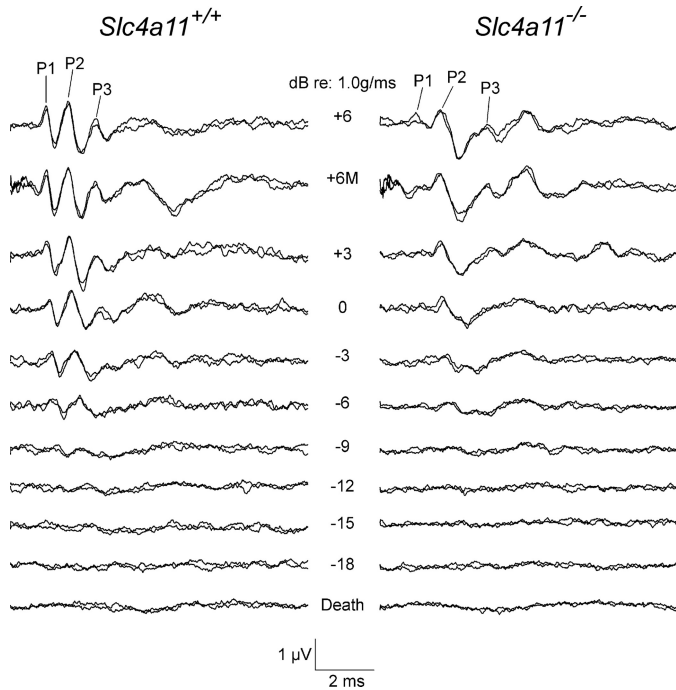
FIGURE 8. **Examples of VsEP waveforms for a typical *Slc4a11*$^{+/+}$ mouse (*left*) and a representative *Slc4a11*$^{-/-}$ mouse (*right*).** Stimuli were calibrated in jerk levels (change in acceleration over time, da/dt) and were defined in terms of db reference 1.0 *g*/ms, where 0 db produced a linear acceleration pulse with jerk amplitude of 1 *g*/ms (g = 9.8 m/s^2). Stimulus amplitudes ranged from +6 db to −18 db. At +6 db, VsEPs were also collected with a forward masker (+6 M group), as described under "Experimental Procedures." Each stimulus level shows two response waveforms to demonstrate response replication. As stimulus intensity is reduced, peak-to-peak amplitudes decrease and latencies increase until no response is visible at levels below threshold. VsEP thresholds for these two animals were scored at −13.5 and −10.5 db for *Slc4a11*$^{+/+}$ and *Slc4a11*$^{-/-}$ mice, respectively.

DISCUSSION

Our results demonstrate that *Slc4a11*$^{-/-}$ mice are an important new model system for addressing the underlying pathophysiology of the sensory abnormalities in patients with NaBC1 mutations (5–14). Prior to the current study, there was no information regarding the expression of NaBC1 protein in the inner ear. We found that NaBC1 was expressed in fibrocytes of the spiral ligament, from the basal to the apical portion of the cochlea, in vestibular fibrocytes, and in corneal endothelial cells, suggesting an important role for electrogenic sodium-coupled borate (or OH$^-$) transport in these cell types. In the mouse cornea, NaBC1 is expressed predominantly in the endothelial cell layer, and the loss of NaBC1-mediated electrogenic ion transport leads to abnormal epithelial and stromal layer morphology.

This is the first study demonstrating the expression of NaBC1 protein in the mammalian cochlea. In an earlier study using a mouse inner ear microarray, *Slc4a11* message was detected in the lateral wall of the cochlea (24). This finding was interpreted as having localized the cotransporter to the stria vascularis (14). However, our results demonstrate that NaBC1 is indeed highly expressed in the lateral wall and localized in spiral ligament fibrocytes rather than the stria vascularis. Cochlear morphology in *Slc4a11*$^{-/-}$ mice showed no alteration in inner and outer hair cells, nerve degeneration, or loss and/or degeneration of spiral ganglia neurons. Therefore, the overall
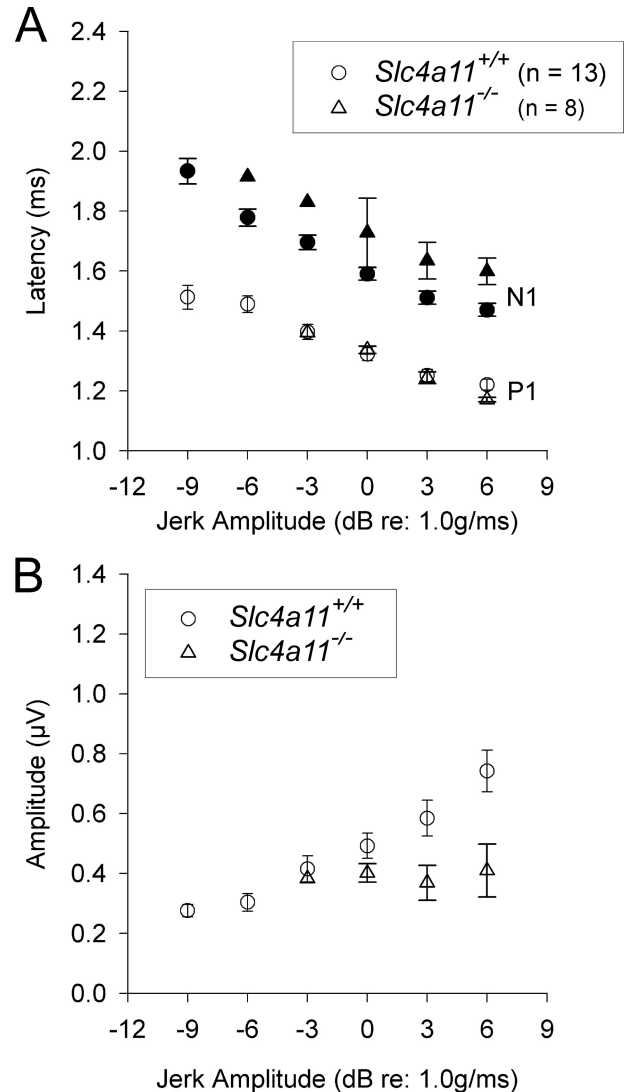

FIGURE 9. *A*, mean VsEP latencies for response peaks P1 and N1. *B*, mean P1-N1 amplitudes as a function of jerk amplitude. N1 latencies were significantly prolonged at all stimulus levels, and P1-N1 amplitudes were significantly smaller in the *Slc4a11*$^{-/-}$ mice. Moreover, the *Slc4a11*$^{-/-}$ mice demonstrated little if any increase in P1-N1 amplitude with increasing stimulus level, whereas the *Slc4a11*$^{+/+}$ mice demonstrated normal amplitude intensity functions. *Error bars*, S.E.

ABR latency delay in *Slc4a11*$^{-/-}$ mice in our study (and by inference Harboyan syndrome) probably results from the lack of NaBC1 in fibrocytes in the spiral ligament. Loss of NaBC1 would result in loss of NaBC1-mediated ion transport and potentially effect the functioning of fibrocytes in the inner ear. An important function of inner ear fibrocytes is to secrete basement proteins located underneath the sensory epithelia, forming part of the extracellular matrix, and the perineural and perivascular basement membranes (25). For this purpose, we determined whether the lack of NaBC1 could impair cochlin secretion (the most abundant protein present in the inner ear, secreted mainly by fibrocytes). However, we did not observe a down-regulation or alteration in cochlin immunostaining in *Slc4a11*$^{-/-}$ mice.

In the present study, ABR data were recorded from two orthogonally oriented electrode pairs using fast sample rates to
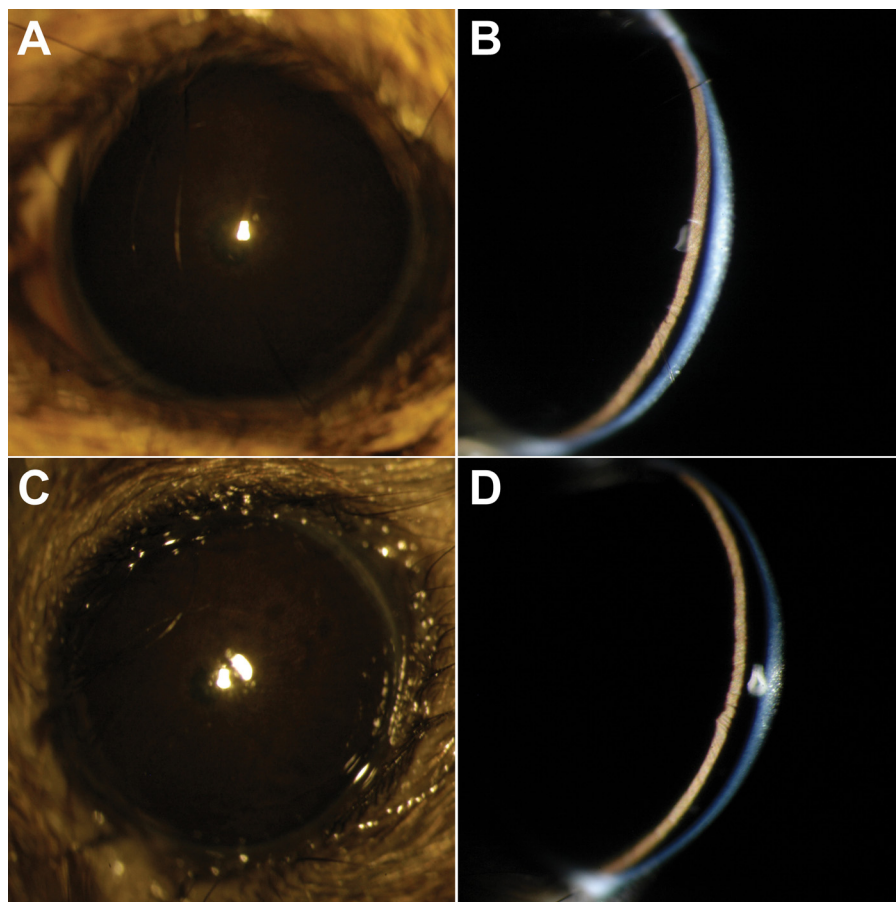
FIGURE 10. **Slit lamp examination of *Slc4a11*$^{+/+}$ (*A* and *B*) and *Slc4a11*$^{-/-}$ (*C* and *D*) mice.** Using diffuse illumination, both *Slc4a11*$^{+/+}$ and *Slc4a11*$^{-/-}$ mice had normal appearing anterior segments without evidence of corneal opacification or edema (*A* and *C*). *B* and *D*, tangentially oriented slit beams confirm that a compact corneal architecture without edema exists in *Slc4a11*$^{+/+}$ and *Slc4a11*$^{-/-}$ mice.

The most dramatic *Slc4a11*$^{-/-}$ result, however, is seen in the pattern of ABR amplitudes in the transverse channel (Fig. 7, *right*). These results clearly document a degenerative process in the auditory periphery as a function of increasing age in these animals. Although the ABR test does not allow us to differentiate precisely between receptor and auditory nerve pathology, these results nevertheless complement our immunohistochemistry and cochlear morphology studies in *Slc4a11*$^{-/-}$ mice, which showed no alteration in inner and outer hair cells, no nerve degeneration or loss, and no degeneration of spiral ganglia neurons; however, there was a lack of NaBC1 immunoreactivity in fibrocytes in the spiral ligament. Thus, it is reasonable to assume that the ABR results seen in *Slc4a11*$^{-/-}$ mice are due primarily to disruption of ionic homeostasis/membrane potentials in the cochlea and not pathology of the eighth nerve. These results support an interpretation that the hearing abnormality in patients with Harboyan syndrome is a disorder of inner ear fibrocytes.

The results also document a hearing deficit of at least 20 db in *Slc4a11*$^{-/-}$ mice. Thus, although control animals show measurable responses down to 55 db (hence their absolute threshold lies below this value), the *Slc4a11*$^{-/-}$ mice fail to show any response at 65 db for all three age groups, and for the older *Slc4a11*$^{-/-}$ mice, their response at 75 db differs little from the 55 db result in controls. Standard audiometric hearing thresholds in human Harboyan syndrome are reported to be elevated 20–50 db at the highest frequency (8,000 Hz) tested (14, 29, 30). Thus, our ABR results are consistent with the human data, although it is difficult to directly compare absolute stimulus intensities. In humans, isolated sensorineural hearing abnormalities have thus far not been reported as a syndrome resulting from *SLC4A11* mutations. The *Slc4a11*$^{-/-}$ mice model (predominant sensorineural hearing loss and mild corneal pathology) suggests that such a syndrome could potentially exist in humans and that NaBC1 mutations should be considered in any patient with familial sensorineural hearing loss who presents with subtle/absent corneal findings.

The collapse of the vestibular membranous labyrinth in *Slc4a11*$^{-/-}$ mice and lack of NaBC1 expression in the stromal fibrocytes in this structure is a novel finding that may explain the nystagmus previously observed in some patients with Harboyan syndrome (14). Nystagmus in these patients has previously been attributed to corneal clouding present from early life (14), yet patients with CHED2 disease do not have nystagmus

accurately measure differences in neural timing. Using this two-channel technique, we have previously shown abnormal auditory responses in two neuropeptide knock-out mouse models: vasoactive intestinal peptide and the related pituitary adenylate cyclase-activating peptide (19). In the mouse, the standard sequence of five positive ABR waves (P1–P5) has been localized to cochlea and/or compound action potential of eighth nerve, cochlear nucleus, contralateral superior olivary complex, lateral lemniscus, and contra lateral inferior colliculus, respectively (26). However, as signals propagate farther along the sensory pathway, the anatomical localization of a particular component becomes more problematic due to such factors as varied central conduction velocities among different classes of auditory neurons, recurrent innervation, refractoriness, fast pathways that bypass some nuclei, etc. (27) as well as increasing variability of single unit firing latencies as one ascends the auditory pathway (28). Our results showed a significant overall latency delay of the initial ABR component in *Slc4a11*$^{-/-}$ mice (averaged across age and ABR channels) due to a significant electrode $\times$ genotype interaction ($p < 0.001$) in which *Slc4a11*$^{-/-}$ mice showed a significantly delayed transverse component (0.97 *versus* 0.77 ms) but relatively faster conduction into central auditory pathways, as reflected in a measure of central conduction time (vertical-transverse; 0.09 *versus* 0.17 ms).
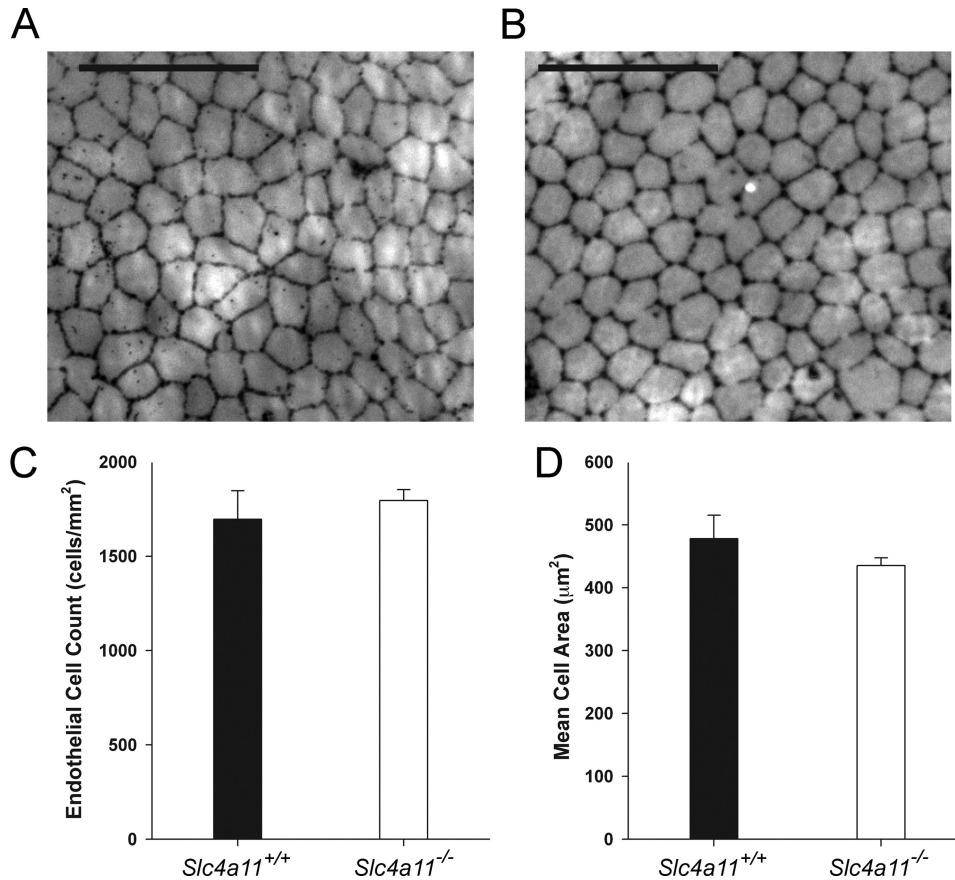
FIGURE 11. *A*, corneal endothelium analysis in *Slc4a11*$^{+/+}$ mice; *B*, corneal endothelium analysis in *Slc4a11*$^{-/-}$ mice. Corneal endothelium was stained with alizarin red to identify cell borders. No gross abnormalities were observed in endothelium from either group. *Scale bar*, 100 μm. Images of alizain red-stained central corneas were used to calculate central endothelial cell densities (*C*) and mean cell area (*D*). No significant differences in cell density or area were observed between *Slc4a11*$^{+/+}$ and *Slc4a11*$^{-/-}$ mouse corneas.

(hydrops)) can evoke nystagmus and vertigo attacks (31) and has been reported in Meniere syndrome in humans (32, 33) and in other mouse knock-out models (34, 35). Based on these considerations, vestibulo-auditory studies in patients with Harboyan syndrome may provide additional clues as to the role of NaBC1 in the inner ear.

The abnormal ABR and VsEP amplitude and latency patterns seen in *Slc4a11*$^{-/-}$ mice (and by inference in Harboyan's syndrome) most likely result from a lack of NaBC1 expression/transport in fibrocytes in the spiral ligament and vestibular stroma. Fibrocytes in the cochlear lateral wall have been implicated as a cause of abnormal ABR amplitudes and hearing abnormalities in various disease states and mouse models (36–38). These ion-transporting cells are known to highly express the Na-K-ATPase and play a major role in K$^+$ recycling, generation of the ~55 mM perilymph-endolymph Na$^+$ gradient, and endochoclear and vestibular electrical potentials (39). Interestingly, stria vascularis and vestibular labyrinth fibrocyte abnormalities are implicated in the hearing abnormalities and vertigo found in mice lacking cochlin, a mouse model for DFNA9 (40). Functional abnormalities of lateral wall fibrocytes also probably play a role in the hearing abnormalities in *Slc4a7*$^{-/-}$ mice, which lack the electroneutral sodium bicarbonate cotransporter NBC3/NBCn1 (18, 41), and in age-dependent hearing loss (42). *Slc4a11*$^{-/-}$ mice not only likely have abnormal fibrocyte NaBC1-mediated transport but, in addition, a collapsed membranous labyrinth in the vestibular region that could add mass to the vestibular end organ, thereby affecting sensory transduction, resulting in elevated VsEP thresholds and latency prolongation.

The corneas in *Slc4a11*$^{-/-}$ mice appeared grossly normal with subtle changes in epithelial cell architecture and a normal endothelium, which remained unchanged as the animals aged. Patients with Harboyan syndrome and CHED2, however, develop corneal edema and opacification at birth. Histological examination and quantitative analysis of corneas taken from patients with CHED2 disease reveals the presence of endothelial cells with normal density but abnormal morphology. Although the endothelial cell layer plays an important role in mediating ion/fluid transport and the hydration status of the cornea, the specific functional role of NaBC1-mediated transport in the endothelium is unknown. What may explain the differences in corneal phenotype between humans and mice deficient for NaBC1, particularly since many of the

despite early similar early onset corneal clouding. The VsEP results in *Slc4a11*$^{-/-}$ mice are consistent with a peripheral pathology affecting the gravity receptor organs. Elevated thresholds suggest that the *Slc4a11*$^{-/-}$ mice have reduced sensitivity of the gravity receptor organs to linear acceleration stimuli. Reduced P1-N1 amplitudes suggest that fewer neurons are responding to the linear acceleration pulse or that the population of responding neurons is not firing with sufficient synchrony to produce a robust compound action potential response peak. Prolonged latencies are suggestive of delayed neural activation or slowed conduction of neural impulses. Given the expression of NaBC1 in the region surrounding the primary afferent dendrites, functional neural deficits seem likely. Despite the neural deficit, balance behavior in the mice was normal, and impaired balance has not been reported in patients. This is probably due to the remarkable capability of the central nervous system to compensate for abnormal peripheral input from the inner ear balance organs.

Our results are therefore compatible with the hypothesis that patients with Harboyan syndrome (and possibly CHED2) may have undiagnosed vestibular pathology and that loss of NaBC1 in stromal fibrocytes in the vestibular apparatus may alter fluid exchange between the perilymphatic (stromal side) and endolymphatic space. An alteration in the membranous labyrinth (collapse or swelling of the endolymphatic space
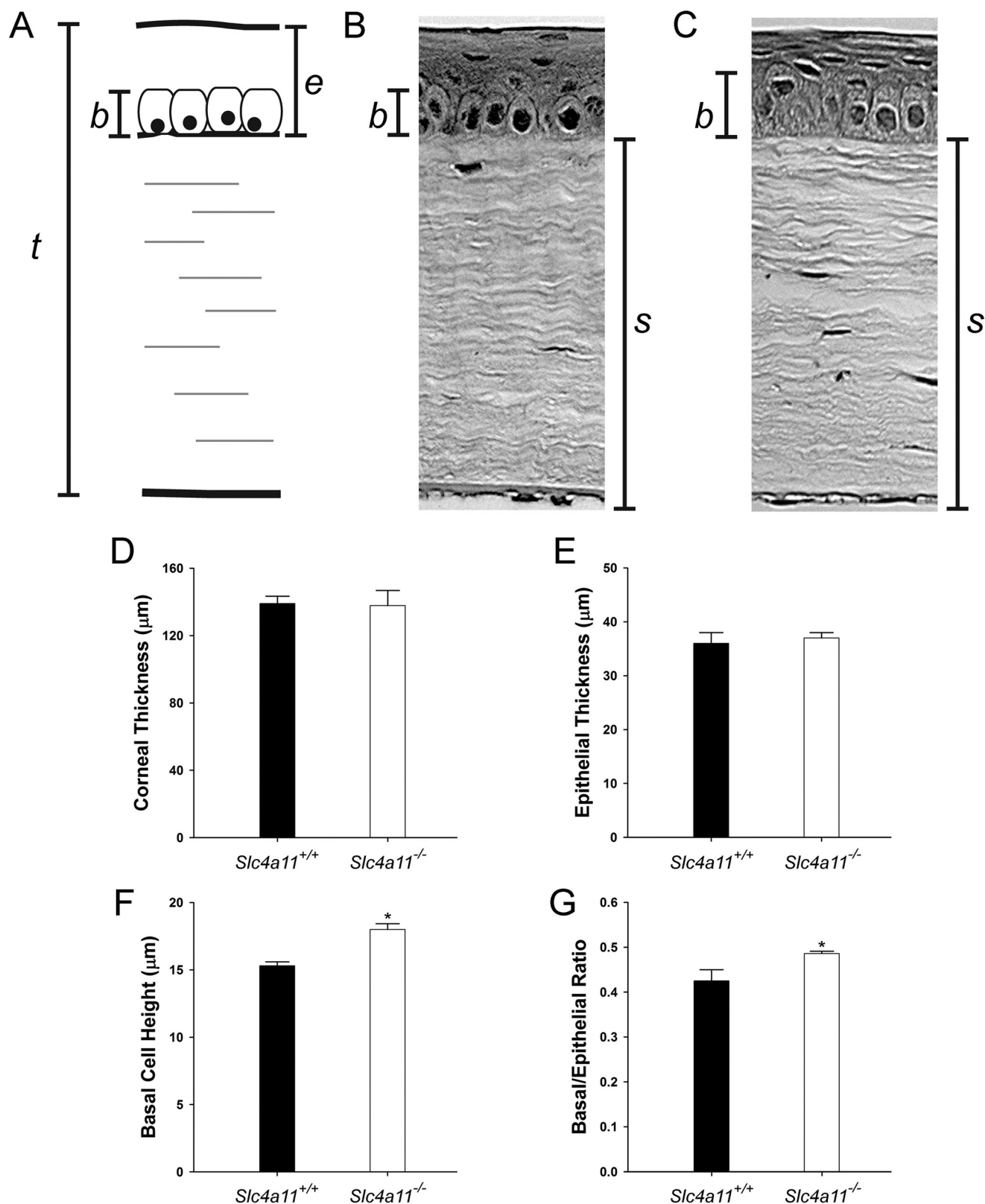
FIGURE 12. **Analysis of hematoxylin and eosin-stained cross-sections from *Slc4a11*$^{+/+}$ and *Slc4a11*$^{-/-}$ mice corneas.** *A*, cross-sections of the central cornea were examined for total thickness (*t*), epithelial thickness (*e*), and the height of the basal epithelial cell layer (*b*). *Slc4a11*$^{+/+}$ (*B*) and *Slc4a11*$^{-/-}$ (*C*) corneal cross-sections have similar total corneal and epithelial thickness. Basal cell height was greater in *Slc4a11*$^{-/-}$ mice. Comparison of corneal architecture in *Slc4a11*$^{+/+}$ and *Slc4a11*$^{-/-}$ mice. Total corneal thickness (*D*) and epithelial thickness (*E*) did not differ significantly between the two groups; however, basal cell height (*F*) and the ratio of basal cell height to epithelial thickness (*G*) were significantly greater (*asterisks*) in *Slc4a11*$^{-/-}$ mice than in *Slc4a11*$^{+/+}$ mice. The stromal layer appeared normal in thickness but more disorganized.
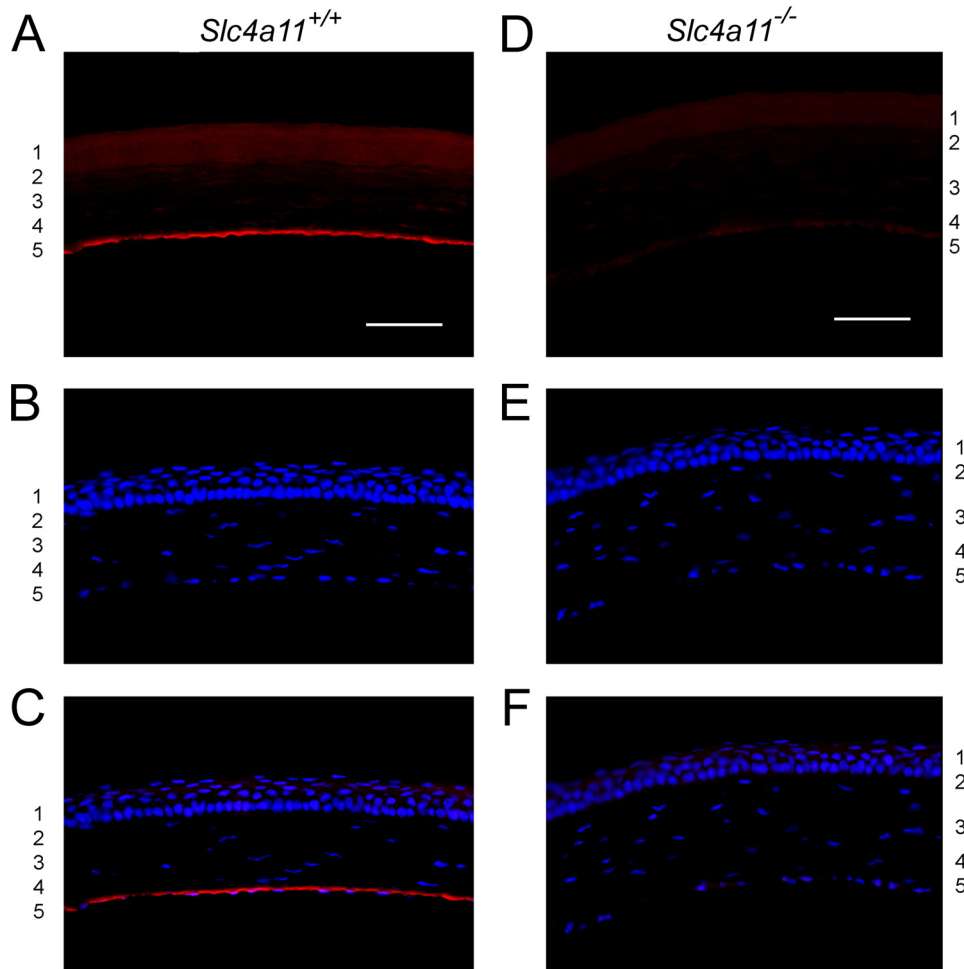
FIGURE 13. **NaBC1 immunofluorescence in *Slc4a11*$^{+/+}$ and *Slc4a11*$^{-/-}$ mouse cornea.** *A*, NaBC1 immunofluorescence was present in layer 5 (endothelium), and less prominent but consistently observed immunofluorescence was seen in *layer 1* epithelium. Much less evident was NaBC1 in the Bowman's (anterior membrane) *layer 2*. No staining was seen in *layers 3* and *4*. *B*, all cell nuclei stained with DAPI. *C*, *merged image* from *A* and *B*. *D*, NaBC1 immunofluorescence was not detected in any corneal layers of the *Slc4a11*$^{-/-}$ mice. *E*, cell nuclei stained with DAPI. *F*, *merged image* from *D* and *E*. *Bar* in *A* and *D*, 20 μm.

The role and requirement of NaBC1-mediated sodium borate transport in mammalian physiology and sensory organs, specifically inner ear fibrocytes and corneal endothelial cells, is currently not known. Evidence exists from *in vitro* studies that borate transport may play a role in eukaryotic cell proliferation (44), but the relevance of this *in vitro* effect is not clear with respect to the development of CHED2 and Harboyan syndrome in humans with mutations in *Slc4a11*. In the eye and inner ear, there are no reported measurements of ambient borate concentrations or studies of borate transport physiology, making it difficult to mechanistically relate the loss of NaBC1 transport activity to the biology of sensorineural tissues. In addition, an essential question that currently has not yet been addressed in the transport literature is whether NaBC1 mediates sodium borate *versus* sodium-hydroxyl cotransport (3) in various tissues or whether NaBC1 has other modes of uncharacterized transport properties. It is also conceivable that the mode of NaBC1 transport varies depending on the ambient borate levels, which may differ in a given tissue and in a species-specific manner. In patients with Fuchs dystrophy, NaBC1 allelic variations have been observed, and a mechanism of ER stress involving the accumulation of aberrantly folded NaBC1 has been proposed (13). In this regard, the NaBC1-deficient mouse model may provide a tool for better understanding of the role of NaBC1 transport in various cell types, given the lack of a specific inhibitor of the cotransporter. Importantly, lessons learned from NaBC1-deficient mice will aid in understanding the mechanisms that prevent murine corneas from undergoing dystrophic changes and provide a better understanding of the molecular and biochemical basis of CHED2, Fuchs dystrophy, and Harboyan syndrome. Finally, the lack of an endothelial phenotype in *Slc4a11*$^{-/-}$ mice despite abnormal corneal epithelial cells allows for a more precise probing of the potential role of NaBC1 in corneal endothelial-stromal-epithelial cell cross-talk.

mutations in the human *SLC4A11* gene that have been described that would be expected to lead to either loss of endothelial NaBC1 expression entirely, or the production of severely truncated forms of NaBC1 that would be expected to have no function? First, mouse and human corneal anatomy and physiology do possess important differences. This includes a substantially thinner cornea lacking a Bowman's layer as well as a corneal endothelium that possesses a replicative potential not observed in human corneas (43). Second, the mouse cornea may be able to compensate for loss of NaBC1 more readily due to these factors or may express other proteins that aid in the compensation. Third, differences in corneal development probably also exist, and if NaBC1 exerts its influence primarily during development, then it may be these differences that are chiefly responsible for the maintenance of corneal clarity in NaBC1-deficient mice. Finally, other factors, such as differences in the level and/or specific corneal cellular localization of NaBC1, differences in NaBC1-protein interaction, and other background gene effects, could play a role in increasing the severity of the corneal phenotype in humans.

REFERENCES

1. Pushkin, A., and Kurtz, I. (2006) *Am. J. Physiol. Renal Physiol.* **290,** F580–F599
2. Parker, M. D., Ourmozdi, E. P., and Tanner, M. J. (2001) *Biochem. Biophys. Res. Commun.* **282,** 1103–1109
3. Park, M., Li, Q., Shcheynikov, N., Zeng, W., and Muallem, S. (2004) *Mol. Cell* **16,** 331–341

4. Takano, J., Noguchi, K., Yasumori, M., Kobayashi, M., Gajdos, Z., Miwa, K., Hayashi, H., Yoneyama, T., and Fujiwara, T. (2002) *Nature* **420,** 337–340

5. Vithana, E. N., Morgan, P., Sundaresan, P., Ebenezer, N. D., Tan, D. T., Mohamed, M. D., Anand, S., Khine, K. O., Venkataraman, D., Yong, V. H., Salto-Tellez, M., Venkatraman, A., Guo, K., Hemadevi, B., Srinivasan, M., Prajna, V., Khine, M., Casey, J. R., Inglehearn, C. F., and Aung, T. (2006) *Nat. Genet.* **38,** 755–757

6. Aldave, A. J., Yellore, V. S., Bourla, N., Momi, R. S., Khan, M. A., Salem, A. K., Rayner, S. A., Glasgow, B. J., and Kurtz, I. (2007) *Cornea* **26,** 896–900

7. Desir, J., Moya, G., Reish, O., Van Regemorter, N., Deconinck, H., David, K. L., Meire, F. M., and Abramowicz, M. J. (2007) *J. Med. Genet* **44,** 322–326

8. Jiao, X., Sultana, A., Garg, P., Ramamurthy, B., Vemuganti, G. K., Gangopadhyay, N., Hejtmancik, J. F., and Kannabiran, C. (2007) *J. Med. Genet* **44,** 64–68

9. Kumar, A., Bhattacharjee, S., Prakash, D. R., and Sadanand, C. S. (2007) *Mol. Vis.* **13,** 39–46

10. Ramprasad, V. L., Ebenezer, N. D., Aung, T., Rajagopal, R., Yong, V. H., Tuft, S. J., Viswanathan, D., El-Ashry, M. F., Liskova, P., Tan, D. T., Bhattacharya, S. S., Kumaramanickavel, G., and Vithana, E. N. (2007) *Hum. Mutat.* **28,** 522–523

11. Sultana, A., Garg, P., Ramamurthy, B., Vemuganti, G. K., and Kannabiran, C. (2007) *Mol. Vis.* **13,** 1327–1332

12. Hemadevi, B., Veitia, R. A., Srinivasan, M., Arunkumar, J., Prajna, N. V., Lesaffre, C., and Sundaresan, P. (2008) *Arch. Ophthalmol.* **126,** 700–708

13. Vithana, E. N., Morgan, P. E., Ramprasad, V., Tan, D. T., Yong, V. H., Venkataraman, D., Venkatraman, A., Yam, G. H., Nagasamy, S., Law, R. W., Rajagopal, R., Pang, C. P., Kumaramanickavel, G., Casey, J. R., and Aung, T. (2008) *Hum. Mol. Genet* **17,** 656–666

14. Desir, J., and Abramowicz, M. (2008) *Orphanet. J. Rare Dis.* **3,** 28

15. Abuin, A., Hansen, G. M., and Zambrowicz, B. (2007) *Handb. Exp. Pharmacol.* **178,** 129–147

16. Joshi, M. A., Jeoung, N. H., Obayashi, M., Hattab, E. M., Brocken, E. G., Liechty, E. A., Kubek, M. J., Vattem, K. M., Wek, R. C., and Harris, R. A. (2006) *Biochem. J.* **400,** 153–162

17. Durocher, Y., Perret, S., and Kamen, A. (2002) *Nucleic Acids Res.* **30,** E9

18. Lopez, I. A., Acuna, D., Galbraith, G., Bok, D., Ishiyama, A., Liu, W., and Kurtz, I. (2005) *Brain Res. Dev. Brain Res.* **160,** 63–77

19. Galbraith, G., Waschek, J., Armstrong, B., Edmond, J., Lopez, I., Liu, W., and Kurtz, I. (2006) *J. Neurosci. Methods* **153,** 214–220

20. Jones, S. (2008) in *Balance Function Assessment and Management* (Jacobson, G. P., and Shepard, N., eds) pp. 379–404, Plural Publishing, San Diego, CA

21. Jones, T. A., and, Jones, S. M. (2007) in *Auditory Evoked Potentials: Basic Principles and Clinical Applications* (Burkard, R. F., Don, M., Eggermont, J. J., eds) pp. 622–650, Lippincott Williams & Wilkins, Baltimore, MD

22. Peyman, G. A., and Spence, D. J. (1977) *Albrecht Von Graefes Arch. Klin. Exp. Ophthalmol.* **201,** 257–261

23. Ping, J., Li, N., Du, Y., Wu, X., Li, L., and Galbraith, G. (2007) *J. Neurosci. Methods* **161,** 11–16

24. Morris, K. A., Snir, E., Pompeia, C., Koroleva, I. V., Kachar, B., Hayashizaki, Y., Carninci, P., Soares, M. B., and Beisel, K. W. (2005) *J. Assoc. Res. Otolaryngol.* **6,** 75–89

25. Mizuta, K., Ikezono, T., Iwasaki, S., Arai, M., Hashimoto, Y., Pawankar, R., Watanabe, T., Shindo, S., and Mineta, H. (2008) *Neurosci. Lett* **434,** 104–107

26. Henry, K. R. (1979) *J. Am. Aud. Soc.* **4,** 173–178

27. Eggermont, J. J. (2001) *Hear. Res.* **157,** 1–42

28. Huang, C. M., and Buchwald, J. S. (1977) *Brain Res.* **137,** 291–303

29. Magli, A., Capasso, L., Foà, T., Maurino, V., and Ventruto, V. (1997) *Ophthalmic Genet.* **18,** 87–91

30. Abramowicz, M. J., Albuquerque-Silva, J., and Zanen, A. (2002) *J. Med. Genet.* **39,** 110–112

31. Handzel, O., Burgess, B. J., and Nadol, J. B., Jr. (2006) *Otol. Neurotol.* **27,** 57–64

32. Ishiyama, G., López, I. A., and Ishiyama, A. (2006) *Curr. Opin. Otolaryngol. Head Neck Surg.* **14,** 332–336

33. Gates, P. (2005) *Intern. Med. J.* **35,** 488–489

34. Megerian, C. A., Semaan, M. T., Aftab, S., Kisley, L. B., Zheng, Q. Y., Pawlowski, K. S., Wright, C. G., and Alagramam, K. N. (2008) *Hear. Res.* **237,** 90–105

35. Rickheit, G., Maier, H., Strenzke, N., Andreescu, C. E., De Zeeuw, C. I., Muenscher, A., Zdebik, A. A., and Jentsch, T. J. (2008) *EMBO J.* **27,** 2907–2917

36. Minowa, O., Ikeda, K., Sugitani, Y., Oshima, T., Nakai, S., Katori, Y., Suzuki, M., Furukawa, M., Kawase, T., Zheng, Y., Ogura, M., Asada, Y., Watanabe, K., Yamanaka, H., Gotoh, S., Nishi-Takeshima, M., Sugimoto, T., Kikuchi, T., Takasaka, T., and Noda, T. (1999) *Science* **285,** 1408–1411

37. Wang, Y., Hirose, K., and Liberman, M. C. (2002) *J. Assoc. Res. Otolaryngol.* **3,** 248–268

38. Delprat, B., Ruel, J., Guitton, M. J., Hamard, G., Lenoir, M., Pujol, R., Puel, J. L., Brabet, P., and Hamel, C. P. (2005) *Mol. Cell. Biol.* **25,** 847–853

39. Lang, F., Vallon, V., Knipper, M., and Wangemann, P. (2007) *Am. J. Physiol. Cell Physiol.* **293,** C1187–C1208

40. Robertson, N. G., Jones, S. M., Sivakumaran, T. A., Giersch, A. B., Jurado, S. A., Call, L. M., Miller, C. E., Maison, S. F., Liberman, M. C., and Morton, C. C. (2008) *Hum. Mol. Genet* **17,** 3426–3434

41. Bok, D., Galbraith, G., Lopez, I., Woodruff, M., Nusinowitz, S., Beltrandel-Rio, H., Huang, W., Zhao, S., Geske, R., Montgomery, C., Van Sligtenhorst, I., Friddle, C., Platt, K., Sparks, M. J., Pushkin, A., Abuladze, N., Ishiyama, A., Dukkipati, R., Liu, W., and Kurtz, I. (2003) *Nat. Genet.* **34,** 313–319

42. Hequembourg, S., and Liberman, M. C. (2001) *J. Assoc. Res. Otolaryngol.* **2,** 118–129

43. Tuft, S. J., Williams, K. A., and Coster, D. J. (1986) *Invest. Ophthalmol. Vis. Sci.* **27,** 1199–1204

44. Park, M., Li, Q., Shcheynikov, N., Muallem, S., and Zeng, W. (2005) *Cell Cycle* **4,** 24–26